Nonlinear Hybrid Plasmonic Waveguides

by

Sarah Aldawsari

A thesis

presented to the University of Waterloo

in fulfillment of the

thesis requirement for the degree of

Master of Science

in

Physics

Waterloo, Ontario, Canada, 2013

© Sarah Aldawsari 2013

AUTHOR'S DECLARATION

I hereby declare that I am the sole author of this thesis. This is a true copy of the thesis, including any required final revisions, as accepted by my examiners.

I understand that my thesis may be made electronically available to the public.

Abstract

Due to the increased demand for high-operating-speed systems and ultra-compact optical devices, nanophotonic waveguides such as plasmonic waveguides have been a subject of intense interest over the past few years. The ability of plasmonic waveguides to guide light within nano-scale structures beyond the diffraction limit has driven researchers in different fields to exploit their unique features. Even though plasmonic waveguides have shown a strong mode confinement at nano-scale dimensions, they have high propagation loss. Consequently, many geometries and structures have been proposed to investigate ways to reduce this loss. The most recent type of plasmonic waveguide that shows high mode confinement and low propagation loss compared with the other types is the hybrid plasmonic waveguide (HPW). An HPW consists of a low-index dielectric layer sandwiched between a high-index dielectric material and a metal layer; the mode is predominantly confined within the low-index layer.

This thesis addresses the use of HPWs for nonlinear applications such as optical switching devices based on the nonlinear phenomenon known as the Kerr effect, where the sub-wavelength dielectric layer has a pronounced nonlinear response. Using Finite Element Method analysis, the nonlinear hybrid plasmonic waveguide (NLHPW) is modeled, and the performance of the NLHPW has been investigated by using appropriate figures of merit to measure the Kerr nonlinearity of the NLHPW with and without the linear loss of the waveguide. These are shown to compare favourably with those of alternate waveguiding geometries. Moreover, the NLHPW has been shown a good balance between mode confinement and loss; small effective mode areas of $0.04 – 0.15\ \mu m^2$ at a wavelength of λ=1.55 μm and relatively long propagation lengths of 30 to 160 μm can be realized, which make NLHPWs promising candidates for nonlinear applications. As a result, a nonlinear ring resonator with a radius of 1 μm based on the NLHPW is designed and investigated numerically by using frequency domain simulations. It is found that the field intensity in the

ring is enhanced four times higher than the field intensity in the input waveguide, and that a nonlinear resonance shift is realized when changing the intensity of the data signal.

Acknowledgements

I would like to express my special thanks to my supervisor **professor Brian West** for his permanent guidance, encouragement, and patience. I was really fortunate to be under his supervision, thanks professor Brian for being a great professor. I would also like to thank my co-supervisor **professor Donna Strickland** and my committee members: **professor Wing-Ki Liu** and **professor Li Wei** for their valuable comments on my thesis.

I am also grateful to my dear mother, **Majeda**, for her support, love, and prayers to me. Certainly, she is the driving force behind any success I achieve in my whole life. I would like also to thank all my **brothers** and **sisters** for their support and encouragement.

I wish to express my deepest gratitude to, my soul-mate, my best friend, my dear husband, **Mohammed** for his peerless love, support, sacrifice, and patience.

Finally, I acknowledge King Abdulaziz University, Saudi Arabia, for their financial support.

Dedication

To my beloved, the greatest parents in the whole world:

My Mother: Majeda

My Father's Soul: Muteb

Table of Contents

AUTHOR'S DECLARATION ii
Abstract iii
Acknowledgements v
Dedication vi
Table of Contents vii
List of Figures ix
Chapter 1 Introduction 1
Chapter 2 Electronic and Photonic Interconnects 3
2.1 Metal Wire Interconnects 3
2.2 Photonic Waveguides 4
Chapter 3 Plasmonic Technology 6
3.1 Background 6
3.1.1 Physics of Surface Plasmon Polaritons 8
3.2 Plasmonic Waveguides 14
3.2.1 Hybrid Plasmonic Waveguides 16
Chapter 4 Nonlinear All-Optical Switching 18
4.1 Optical Switches 18
4.2 The Importance of Nonlinear Optical Switching 19
4.3 Nonlinear Optical Waveguides 20
Chapter 5 Methodology and Analysis 23
5.1 Finite Element Method 23
5.2 Nonlinear Hybrid Plasmonic Waveguide 24
5.2.1 Waveguide Structure 24
5.2.2 Method of Analysis 25
5.2.3 Modeling Procedure 28
5.2.4 Simulation Results 30
5.3 Nonlinear Ring Resonator Device 36

5.3.1 Modeling Procedure 36
5.3.2 Device Analysis 40
5.3.3 Results and Discussion 41
Chapter 6 Conclusion and Future Steps 46
APPENDICES 48
Appendix A: Mode-Solving Simulation Report 49
Appendix B: Frequency Domain Simulation Report 69
Appendix C: Matlab Code of 2D Scan 92
Bibliography 98

List of Figures

Figure 1: Dimension and operating speed of electronic, photonic, and plasmonic devices [10]. 7

Figure 2: (right) the dispersion curve shows the momentum mismatch issue, (left) SPPs at the interface of metal and dielectric materials [12] 8

Figure 3: The optical mode in (a) V-groove, and (b) MIM plasmonic waveguides [26,30]. ... 15

Figure 4: (left) The hybrid plasmonic waveguide geometry, (right) the hybrid optical mode is confined in the sub-wavelength small index gap [35]. 17

Figure 5 : The proposed geometry of the NLHPW. 25

Figure 6: Previous NLHPW geometries: (a) non-planar [58], and (b) planar[60]. 28

Figure 7: (right) The field distribution for E_y of the hybrid fundamental mode; (left) 1D plot for the $E_y(0,y)$. 30

Figure 8: The effect of the metal film thickness on $A\text{eff}, Lp, n2, \gamma$, and F, where the HPW parameters are $HS = W$= 250 nm, and $\boldsymbol{t}$=10 nm. 31

Figure 9: The effect of the cover indices (air,blue) and (SiO2, black dotted) on the A_{eff}, n_2, γ, and F when the HPW parametres are t= 10 nm, H_S=250 nm, and H_M= 200 nm..... 33

Figure 10: The effect of the ridge height for different values of thickness t=10, 20, 30, 40, and 50 nm on the values of A_{eff}, n_2, Lp $\boldsymbol{\gamma}$, and F. 34

Figure 11: The variation of F with HS and W, the black dot represents the optimized value of $F = 2.32 \times 106\ \mu\text{m}/(\text{W} \cdot \text{m})$ when $HS = 246$ and $W = 182$ nm..... 35

Figure 12: The variation of γ with HS and W, the black dot shows that the maximum value of $\gamma = 7.64 \times 104(\text{W} - 1 \cdot \text{m} - 1)$ is found at $HS = 174$ and $W = 258$ nm. 36

Figure 13: A schematic diagram of the effective index method applied on the NLHPW. 38

Figure 14: A 2D plot for the electric field $\boldsymbol{Ez}$ in the waveguide, where the *x* and *y* axes represent the computational domain of the waveguide in microns..... 39

Figure 15: A 1D plot for the power flow in the x-direction of the waveguide. 39

Figure 16: A schematic diagram of the nonlinear ring resonator device. 41

Figure 17: A surface plot shows the power flow in the *x*-direction of the ring resonator device at the resonance, where the intensity in the ring is enhanced 4 times more than the input waveguide, the horizontal and vertical axes represent the computational domain in microns. 43

Figure 18: The transmission spectrum of the nonlinear ring resonator device; it shows the FSR, FWJM, and the depth of the resonance peak at $\sim$ 1.55 μm..... 44

Figure 19: (left) The nonlinear resonance shift of the ring resonator transmission for different input powers; (right) the shift in nonlinear resonance wavelengths increase as input power increases..... 45

Chapter 1
Introduction

Since the invention of the first transistor in 1947 [1], the technology of electronic circuits has developed rapidly. The transistor is considered an important element in modern computers for its superior functionalities to switch on/off or to amplify electrical signals in electronic integrated circuits. Due to advances in nano-fabrication techniques, the number of transistors in electric circuits has increased significantly, and their size has shrunk to the nano-scale. Therefore, many logic operations are performed electronically in integrated circuits with little power consumption. In addition, miniaturization of integrated circuit components has led to minimizing the electrical interconnects that usually are made from metals for transferring data from one element to another in the chip.

However, scaling on-chip metal wire interconnects down to the nano-scale has several disadvantages due to the physical restrictions related to charging and discharging metal wires electrically such as signal latency, power dissipation, and cross-talk [2]. These problems need to be addressed by the current advanced technology due to the ever-increasing demand for high-speed information processing. Currently, there is an increasing interest in optical telecommunications and network systems to transmit data as optical signals. Processing and routing of data still occurs in the electronic domain because all-optical switches are not yet highly evolved. This results in the other critical issue facing high-speed signal processing and electronic switching – the "electronic bottleneck" [3].

To overcome these issues, much research has been conducted with a goal to transmit and route data in the optical domain, so that signals can be processed all-optically rather than relying on optical-electrical-optical (OEO) conversion. The scientific field that studies generating, transmitting, amplifying, switching, and detecting light is called *photonics*, a branch of optics. The reason for this trend towards photonic technology is to exploit the excellent properties of photons rather than electrons. Light waves have very

broad bandwidth; this means that a large amount of data can be transmitted through optical interconnects in a given time interval. For example, in optical communication systems, optical fibers can convey information with a capacity 1000 times greater than the carrying capacity of electronic interconnects [4]. In addition, electromagnetic waves have low propagation loss and high immunity to electromagnetic interference and cross-talk [5]. Therefore, optical interconnects can be used to overcome the aforementioned limits of electronic interconnects. However, minimizing the size of on-chip optical interconnects presents the diffraction limit, which dictates that light cannot be confined in a region with linear dimension less than half its wavelength in the material. This issue makes electronics successful in entering the nano-scale world before photonics.

Plasmonic technology – a branch of nanophotonics – has offered a solution to the diffraction limit problem so that scaling photonic components such as waveguides on-chip down to the nano-scale can be possible. Therefore, due to this feature of plasmonics, it is predicted that photonic chips will replace electronic chips once the former's propagation loss is optimally reduced. Consequently, much attention has been paid to nano-scale plasmonic waveguides, particularly how we can minimize the propagation loss by proposing different types of geometries and structures. In our work, we shall focus on modeling nonlinear nano-plasmonic waveguides and using them to model an all-optical switching nano-scale resonator device, where the nonlinearity is a very important factor to achieve all-optical information processing.

Chapter 2
Electronic and Photonic Interconnects

With the quick progress of nano-fabrication techniques, electronic integrated circuits have been developed rapidly, resulting in revolutionary developments in nano-scale electronic devices such as nanotransistors, which are the building block of integrated circuits. Due to the physical limitations of metallic nano-wire interconnects, the operating speed of electronic devices has been limited to the gigahertz range. Nanophotonic technology can provide the solution to this problem by exploiting the beneficial features of photonic and electronic technologies and integrating them on the same chip. This chapter is divided into two sections: the achievements and limitations of metal wire interconnects, and those of conventional photonic waveguides.

2.1 Metal Wire Interconnects

Conductive metal wire interconnects are considered important elements on electronic integrated circuits. Interconnects have several functions in electronic devices, described here in order of increasing scale. One type of interconnects links the elementary devices such as transistors, resistors, and capacitors to transmit electrical signals among them. Another type connects the essential parts of the electronic circuits such as the processor and the memory. Interconnects that join chips on the same board are a third type, while board-to-board connections form a fourth. Plasmonic technologies are envisioned for the first two (and possibly three) of these applications. One of the important features of metal wire interconnects is the possibility of scaling them down to the nano-scale so that millions of electronic devices can be integrated on a single chip. The other feature is that metal interconnects on the electronic circuit can be bent and have sharp corners because electrons move in metals with negligible bending loss.

When electronic components on electronic circuits are reduced in size, the performance of transistors increases, whereas the performance of nano-metallic wires decreases because of various physical constraints resulting from charging and discharging

metal wires. Scaling the cross-sectional area of metal wire interconnects down to the nano-scale results in an increase of the interconnects' resistance. Therefore, the time delay of electrical signals, which is the product of the resistance and capacitance of the metal, will increase. As a result, the operating speed of electronic circuits is limited to the gigahertz range. Another issue that arises from increasing the resistance of metallic nano-wires is power dissipation. Some of the power will be transmitted through the metal wires and the rest will be lost through Joule heating due to the increase of resistance. Crosstalk among metal wire interconnects is also problematic; it is a common phenomenon that happens when wires are close to one another. The electrical signals of close wires are disturbing one another resulting in unwanted capacitive coupling [2]. For example, when a wire transmits an electrical signal, and this wire is close to another wire that called a victim wire, the potential difference on the victim wire will be changed, resulting in a current flow. These physical limitations of minimizing metal interconnects have driven researchers to find ways to help address these issues such as finding metal materials with low resistance or using optical interconnects instead of metal wires.

2.2 Photonic Waveguides

Structures that can guide and confine electromagnetic waves in two dimensions while allowing them to propagate along the third dimension are called photonic waveguides. The mechanism of controlling light within these structures depends on the core and cladding refractive indices and the incident angle of electromagnetic waves into the core. Light can be confined within the core when the core refractive index is higher than the cladding index and when the total internal reflection (TIR) principle occurs, which can be understood easily from Snell's law. Many geometries have been proposed and fabricated at the micro-scale to guide and transmit light. Some, such as optical fibers and channel waveguides, are based on the TIR principle, whereas others, such as photonic crystals and slot waveguides, do not rely on it.

However, TIR photonic waveguides encounter two obstacles, so minimizing them to the nano-scale and keeping the same functionality is difficult. The first limitation is that light cannot be guided around sharp corners. When the core is bent, light tends to radiate into the cladding region, resulting in bending loss [6]. Bending loss occurs when the TIR condition no longer holds. This bending loss depends on the curvature radius, and this curvature radius should exceed a critical radius in order to keep the bending loss low. Critical radii depend on the difference between the refractive indices of the core and the cladding of the waveguide. The critical radius is small when the index difference is high – an example is the silicon waveguide, which has a critical radius of a few microns [7]. On the other hand, when the index difference is low, the critical radius is large; for example, glass waveguides have critical radii of a few millimeters [8]. Bending loss increases severely when the curvature radii decrease below the critical value. Bent waveguides are important components in photonic integrated circuits (PICs) such as ring resonators, and this high bending loss at small radii makes designing nano-bent waveguides problematic.

The second limitation is that light waves cannot be confined in a region with a dimension less than half their wavelength in the material; this phenomenon is called the diffraction limit. In order to conform to the diffraction limit, the core transverse dimensions d_x and d_y of a dielectric waveguide should be

$$d_x, d_y \geq \frac{\lambda}{2n_{\text{core}}}, \tag{1}$$

where λ is the free space wavelength, and n_{core} is the core refractive index [9]. This diffraction limit represents a critical barrier to nano-photonic chip technology.

Chapter 3
Plasmonic Technology

Metallic nano structures such as nano-particles and thin metal films have received much interest because of the current development of nano-fabrication techniques and the unique properties of nano-materials. The technology that studies the interactions between light and nanometallic structures is called plasmonics. It can be seen from Fig. 1 how this technology takes the best features of both electronic and photonic technologies [10], so it is a promising technology for the future of chips. The optical properties of metallic structures at the nano-scale are different from those of bulk metals. For example, when light is incident on the surface of good conductor nano-particles (that have a high density of free electrons), the light oscillates with these free charges resulting in absorbing or scattering light with different colors that depends on the surface shape and size of nano-particles. The earliest example of this phenomenon is the Roman glass cup "Lycurgus" that contains gold nano-particles [11]. When light is shone through the cup, the transmitted light is a bright red because of the transparency of gold nano particles to the longer wavelengths whereas the cup shines green when illuminated in reflection due to the scattering of the shorter wavelengths. In this chapter, some background of plasmonics and some applications such as plasmonic waveguides will be discussed.

3.1 Background

Plasmonics is an emerging field of nanophotonics in which light is controlled and guided beyond the diffraction limit by exploiting the unique optical properties of metal-dielectric interfaces. When electromagnetic waves are incident at such an interface under certain conditions, the light will be coupled to electron density oscillations at the surface, thereby forming electromagnetic waves that propagate along the surface called surface plasmon polaritons (SPPs) [12]. In the past, there were many pioneering studies about surface plasmons and ways to excite them. Early studies were performed by Ritchie in 1957. He theoretically proved that surface plasmons exist by studying the energy losses incurred

when fast electrons pass through a thin metal foil [13]. Two years later, SPs were observed experimentally by Swan and Powell, also by conducting who conducted experiments on the electron energy loss of metals [14].

Many techniques have been proposed to excite SPs. In the late 1960s, some methods based on prisms were proposed to excite SPs optically [15-17]. For example, the Otto method involves fixing a prism near to a dielectric-metal interface, where the separation distance is on the order of one wavelength. The excitation of SPs occurs via the evanescent wave resulting from total internal reflection at the prism-dielectric interface. Using gratings is another way to excite SPPs, wherein a metal film is deposited on the grating surface [18-19]. When photons are incident on the grating, the excited SP modes will have a momentum of $2\pi h/a$, where a is the grating period, which is greater than that of the incident photons.

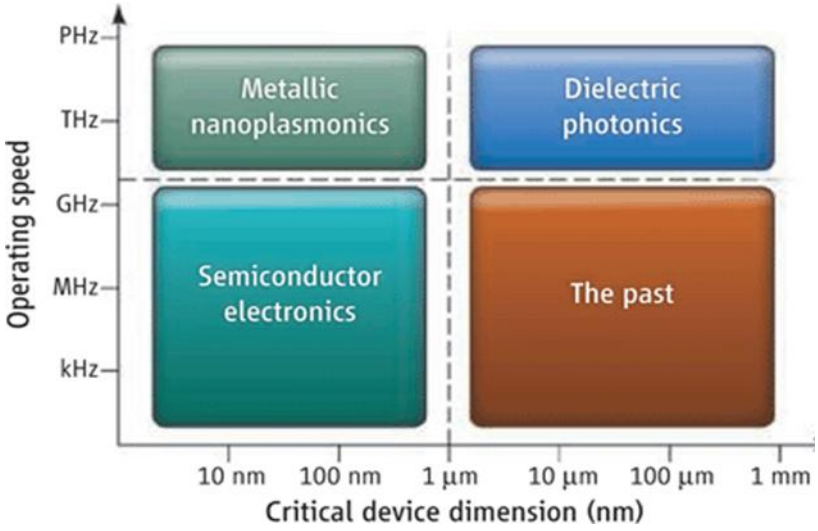


Figure 1: Dimension and operating speed of electronic, photonic, and plasmonic devices [10].

3.1.1 Physics of Surface Plasmon Polaritons

Conductive materials have a specific density of free electron densities, the collective oscillations of which are called plasmons. When confined at a metal-dielectric interface, they are called surface plasmons. As illustrated in Fig. 2, these surface plasmons generate a strong electric field normal to the interface. The coupling between SPs and light generates surface plasmon polaritons (SPPs) that are, as mentioned before, electromagnetic waves propagating along the metal-dielectric interface and decaying exponentially in the directions normal to the surface [12].

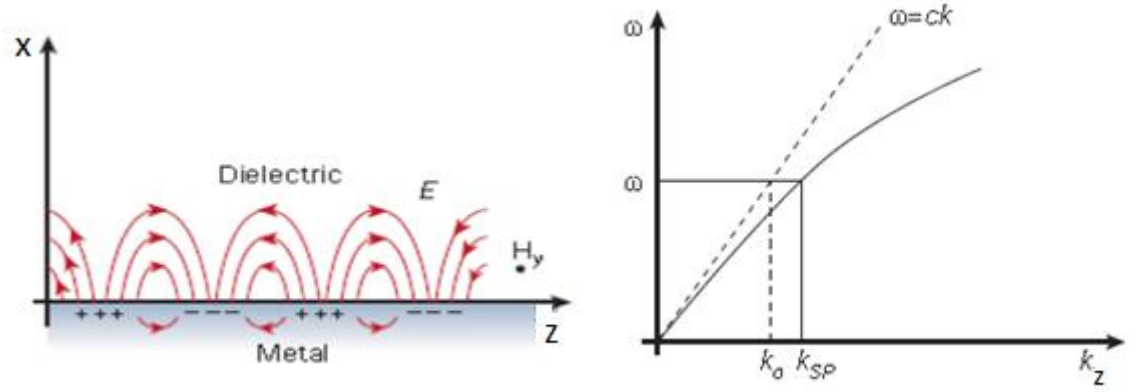


Figure 2: (right) the dispersion curve shows the momentum mismatch issue, (left) SPPs at the interface of metal and dielectric materials [12] .

The SPP modes and their dispersion relation can be derived by using Maxwell's equations with suitable boundary conditions [20-21].The wave equation must be applied to determine the mode profiles and polarization properties of SPP modes. The solution of the wave equation must produce a propagating wave that is localized to the metal-dielectric interface, decaying exponentially in both perpendicular directions to the interface. We choose a simple structure of a single metal-dielectric interface as shown in Fig. 2. Here, the dielectric permittivity ε_d is considered to be a real and positive quantity due to the near lossless nature of dielectric materials, and the metal permittivity is a complex-valued

function ε_m. We neglect dispersion in the dielectric constants. The wave equation for electric field in a bulk medium with permittivity ε is

$$\nabla^2\vec{\mathrm{E}} + k_0^2\varepsilon\vec{\mathrm{E}} = 0, \tag{2}$$

where k_0 is the wavenumber in vacuum. The propagating modes can be described as $\vec{\mathrm{E}}(x,y,z) = \vec{\mathrm{E}}(x)e^{i\beta z}$, where β is the complex propagation constant of the travelling waves in the direction of propagation. The field has no *y* dependence, as the geometry is assumed infinite in this direction. By substituting the expression of the electric field into Eq. (2), the wave equation can be rewritten as

$$\frac{\partial^2\vec{\mathrm{E}}(x)}{\partial x^2} + (k_0^2\varepsilon - \beta^2)\vec{\mathrm{E}} = 0; \tag{3}$$

similarly, the wave equation for magnetic field is

$$\frac{\partial^2\vec{\mathrm{H}}(x)}{\partial x^2} + (k_0^2\varepsilon - \beta^2)\vec{\mathrm{H}} = 0. \tag{4}$$

For transverse magnetic (TM) modes, the magnetic field has only one component: $\vec{\mathrm{H}} = H_y(x)e^{i\beta z}\hat{\mathrm{y}}$, where

$$H_y(x) = \begin{cases} Ae^{-k_d x}, & x > 0 \\ Be^{k_m x}, & x < 0 \end{cases}, \tag{5}$$

where k_d and k_m are the wave number components of the decaying fields into the two materials in a perpendicular direction to the interface. The reciprocal of these components gives the decay distance of the fields; those components must have a positive real part in order to have the fields confined to the interface.

By using Ampère's equation for time-harmonic fields,

$$\nabla \times \vec{\mathrm{H}} = -i\omega\varepsilon\vec{\mathrm{E}}, \tag{6}$$

the electric field components can be written as

$$\vec{\mathrm{E}} = \frac{1}{i\omega\varepsilon}\left(i\beta H_y\hat{\mathrm{x}} - \frac{\partial H_y}{\partial x}\hat{\mathrm{z}}\right), \tag{7}$$

where the non-vanishing electric field components are E_z and E_x.

By applying Eq. (4) for the upper half-plane of Fig. 2, $x > 0$, the solutions are

$$H_y(x,y,z) = Ae^{i\beta z}e^{-k_d x}, \tag{8}$$

$$E_z(x,y,z) = iA\frac{1}{\omega\varepsilon_0\varepsilon_d}k_d e^{i\beta z}e^{-k_d x}, \tag{9}$$

and

$$E_x(x,y,z) = -A\frac{\beta}{\omega\varepsilon_0\varepsilon_d}e^{i\beta z}e^{-k_d x}. \tag{10}$$

For the lower half plane , $x < 0$, the solutions are

$$H_y(x,y,z) = Be^{i\beta z}e^{k_m x}, \tag{11}$$

$$E_z(x,y,z) = iB\frac{1}{\omega\varepsilon_0\varepsilon_m}k_m e^{i\beta z}e^{k_m x}, \tag{12}$$

and

$$E_x(x,y,z) = -B\frac{\beta}{\omega\varepsilon_0\varepsilon_m}e^{i\beta z}e^{k_m x}. \tag{13}$$

The continuity of the electric and magnetic field components that parallel to the surface and the normal components of the electric displacement εE_x at the plane $x = 0$ requires that

$$A = B \quad \text{and} \quad A\frac{k_d}{\varepsilon_d} = -B\frac{k_m}{\varepsilon_m}. \tag{14}$$

Since $A = B$, we get

$$\frac{k_m}{k_d} = -\frac{\varepsilon_m}{\varepsilon_d}. \tag{15}$$

The wave vector of the decaying field in the metal k_m is a complex function, but it must have a positive real part, whereas the wave vector of the field in the dielectric material k_d must be real and positive, since the dielectric is lossless. Therefore, the requirement in

order to have SPs at a metal-dielectric interface is that the relative permittivities of metal and dielectric should be opposite in the sign of their real part. The permittivity of a dielectric is positive real due to its near-lossless nature, and some metals have negative real permittivities at optical frequencies, which can be calculated from the Drude model [20]. Unlike dielectric materials, metals have complex permitivities $\varepsilon_m = \varepsilon_m' + i\varepsilon_m''$; the imaginary part due to the lossy nature of metals. Therefore, SPP modes can have TM polarization.

For the transverse electric (TE) mode, the electric field has only one component: $\vec{\mathbf{E}} = E_y(x)e^{i\beta z}\hat{\mathrm{y}}$. By using Faraday's law for time-harmonic fields,

$$\nabla \times \vec{\mathrm{E}} = i\omega\mu_0\vec{\mathrm{H}}, \tag{16}$$

the non-vanishing magnetic field components are H_z and H_x, where μ_0 is the magnetic permeability of free space.

By applying Eq. (3) for the upper half-plane of Fig. 2, $x > 0$, the solutions are

$$E_y(x,y,z) = Ae^{i\beta z}e^{-k_d x}, \tag{17}$$

$$H_z(x,y,z) = -iA\frac{1}{\omega\mu_0}k_d e^{i\beta z}e^{-k_d x}, \tag{18}$$

and

$$H_x(x,y,z) = A\frac{\beta}{\omega\mu_0}e^{i\beta z}e^{-k_d x}. \tag{19}$$

For the lower half-plane of Fig. 2, the solutions are

$$E_y(x,y,z) = Be^{i\beta z}e^{k_m x}, \tag{20}$$

$$H_z(x,y,z) = iB\frac{1}{\omega\mu_0}k_m e^{i\beta z}e^{k_m x}, \tag{21}$$

$$H_x(x,y,z) = B\frac{\beta}{\omega\mu_0}e^{i\beta z}e^{k_m x}. \tag{22}$$

The continuity of the field components at the plane $x = 0$ requires that

$$A = B \quad \text{and} \quad Ak_d = -Bk_m. \tag{23}$$

Since $A = B$, we get

$$A(k_d + k_m) = 0. \tag{24}$$

In order to have SPP modes confined to the surface, k_d and k_m should have real positive parts; that means, A should equal zero, which leads to $A = B = 0$. Therefore, there is no non-trivial solution for TE-polarized SPP modes. In other words, SPP modes only have TM polarization.

To find the dispersion relation of SPP modes, the $\hat{y}$ components of the magnetic field can be substituted in Eq. (4), and k_m and k_d can be written as

$$k_m^2 = \beta^2 - k_0^2 \varepsilon_m \tag{25}$$

and

$$k_d^2 = \beta^2 - k_0^2 \varepsilon_d. \tag{26}$$

After substituting Eq. (15) into Eqs. (25-26), the dispersion relation of SPP modes can be written as

$$k_{spp} = k_0 \sqrt{\frac{\varepsilon_m \varepsilon_d}{\varepsilon_m + \varepsilon_d}}. \tag{27}$$

From this relation, it can be seen that the wave number of SPPs depends critically on the optical properties of the metal and dielectric materials; ε_m and ε_d, respectively. The wave number k_{spp} is a complex function, $k_{spp} = k'_{spp} + ik''_{spp}$ since ε_m is a complex value. Hence, Eq. (27) can be written as

$$k_{spp} = k_0 \sqrt{\frac{\varepsilon_d \varepsilon'_m \left(1 + \frac{i\varepsilon''_m}{\varepsilon'_m}\right)}{\varepsilon_d + \varepsilon'_m \left(1 + \frac{i\varepsilon''_m}{\varepsilon'_m + \varepsilon_d}\right)}}. \tag{28}$$

Since the contribution of ε''_m is small comparing to ε'_m, the assumption $|\varepsilon''_m| \ll |\varepsilon'_m|$ can be used. In addition, using square root Taylor expansion to the first order($\sqrt{1+x} = 1 + \frac{x}{2}$), Eq. (28) can be written as

$$k_{spp} = k_0\sqrt{\frac{\varepsilon_d\varepsilon_m'}{\varepsilon_d+\varepsilon_m'}}\cdot\frac{[1+\frac{i\varepsilon_m''}{2\,\varepsilon_m'}]}{[1+\frac{i\varepsilon_m''}{2(\varepsilon_m'+\varepsilon_d)}]} \tag{29}$$

$$= k_0\sqrt{\frac{\varepsilon_d\varepsilon_m'}{\varepsilon_d+\varepsilon_m'}}\cdot\frac{\left[1+\frac{i\varepsilon_m''}{2\,\varepsilon_m'}-\frac{i\varepsilon_m''}{2(\varepsilon_m'+\varepsilon_d)}+\frac{{\varepsilon_m''}^2}{4\varepsilon_m'(\varepsilon_m'+\varepsilon_d)}\right]}{\left[1+\frac{i{\varepsilon_m''}^2}{4(\varepsilon_m'+\varepsilon_d)^2}\right]}. \tag{30}$$

By neglecting the second order terms of ε_m'', the real part of SPP mode wavenumber can be written as

$$k_{spp}' = k_0\sqrt{\frac{\varepsilon_m'\varepsilon_d}{\varepsilon_m'+\varepsilon_d}}, \tag{31}$$

and the imaginary part is

$$k_{spp}'' = \frac{k_0}{2}\frac{\varepsilon_m''}{\sqrt{\varepsilon_m'}}\left(\frac{\varepsilon_d}{\varepsilon_m'+\varepsilon_d}\right)^{\frac{3}{2}}. \tag{32}$$

The real part indicates the wavelength of the SPP mode, whereas the imaginary part provides information about their propagation loss [22]. When the imaginary part of the SPP modes increases, the propagation length – the distance over which the propagating power decays to $1/e$ of its initial value – will decrease. Therefore, the wavelength and the propagation length of SPP mode can be written as

$$\lambda_{spp} = \frac{2\pi}{k_{spp}'} = \frac{2\pi}{k_0}\sqrt{\frac{\varepsilon_m'+\varepsilon_d}{\varepsilon_m'\varepsilon_d}}, \tag{33}$$

and

$$L_{spp} = \frac{1}{2k_{spp}''}. \tag{34}$$

From Eq. (31), the wavenumber of SPP modes k_{spp}' is greater than the wavenumber of free space light k_0 at the same frequency so that free space light cannot couple directly to SPs due to momentum mismatch between them. This mismatching in momentum issue can be tackled by using special techniques, some of them mentioned in the previous section. Since the field intensity of SPP modes is maximized and localized at the metal-dielectric interface and decaying exponentially away from the interface, SPP modes do not have a diffraction limit like TIR photonic waveguides, where the confined modes are subject to the diffraction

limit. SPP wavelength can be made arbitrary small when ε_m' and ε_d are nearly equal in magnitude because SPP wavelength depends on the optical properties of the materials as seen from Eq. (33).

3.2 Plasmonic Waveguides

Due to the tremendous progress in nano-fabrication techniques such as electron-beam lithography, ion-beam milling, and self-assembly, the advancements in nano-characterization techniques such as near-field optical spectroscopies, and the higher performance of current electromagnetic simulation tools [11,23], there has been much interest in investigating plasmonic devices. For example, chemists and biologists have conducted much work to use plasmonic devices in bio-sensing [24,25]. In addition, physicists and engineers have paid much attention to optical devices such as plasmonic waveguides because of their ability to confine light beyond the diffraction limit. Many plasmonic waveguiding sub-wavelength channel structures and geometries have been proposed and investigated numerically and experimentally. For example, V-grooves [26, 27] are channel plasmonic waveguides where the metal surface is carved into v-shapes; the field distribution of the v-groove waveguide is maximized at the interface of the metal-dielectric as shown in Fig. 3(a). V-grooved structures have not only been used as optical interconnects but also as optical switches such as resonators [28]. Metallic stripes are other structures that confine light at sub-wavelength scale; these are also called insulator-metal-insulator (IMI) waveguides. In addition, metal-insulator-metal (MIM) waveguides are other structures of plasmonic waveguides. Both IMI and MIM waveguides have been studied at different wavelengths [26-30]. In an MIM waveguide structure; also called a gap plasmonic waveguide, the confined mode, as shown in Fig. 3(b), results from the coupling between the SPPs at the two surfaces. As opposed to dielectric waveguides, MIM structures have shown the potential for use in bends and power splitters at telecom wavelengths without excess loss resulting from the bending [31]. IMI waveguide structures support what are known as long range surface plasmon polaritons (LRSPP) because their propagation lengths are

considerably longer than those of single-surface metal-dielectric waveguides [32-34]. On the other hand, the optical mode of MIM waveguides is more confined than the IMI waveguide mode [29]. The best way to test whether the waveguide performs optimally or not is to calculate the propagation length of propagating modes and the degree of mode confinement. Unfortunately, there is a trade-off between mode confinement and propagation loss. All plasmonic waveguides suffer from propagation loss that is a critical issue affecting the progress of plasmonic technology; this loss comes from the fact that metals are lossy at optical frequencies. A good optical confinement, where the mode is highly confined within the waveguide core, is an important feature of waveguides, which link the optical devices on photonic integrated circuits. Weakly-confined waveguides may lead to cross-talk among parallel optical interconnects and affect the transmitted signals. For high-density photonic integrated circuits, there is a need for devices with strong sub-wavelength optical mode confinement and low propagation loss. Consequently, there have been many attempts to balance between loss and mode confinement in plasmonic waveguides by proposing different geometries and structures. The one that most successfully has shown a good balance between loss and confinement will be discussed in the next section.

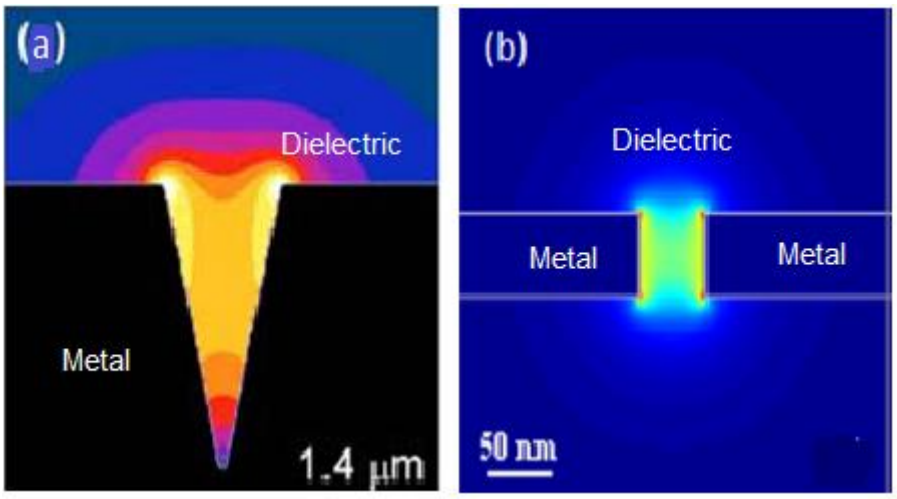


Figure 3: The optical mode in (a) V-groove, and (b) MIM plasmonic waveguides [26,30].

3.2.1 Hybrid Plasmonic Waveguides

Some of the waveguides have shown strong confinement but have short propagation lengths of a few microns, which is not practical for device applications [29]. For this reason, a great deal of research has been done to solve this issue by proposing different geometries and structures. One pioneering work was done in 2008 by Oulton *et al*.; they proposed a novel plasmonic waveguide geometry that shows a good balance between propagation length and mode confinement in two dimensions [35]. Their geometry – shown in Fig. 4 – is a combination of a conventional dielectric slot waveguide and a plasmonic waveguide, which consists of a sub-wavelength dielectric low-index nano-gap (SiO_2) sandwiched between a metallic region (silver) and high index dielectric nanowire (GaAs). By controlling the dimensions of the geometry such as the nanowire radius d and the gap width h, the optical mode which is shown in Fig. 4 will be confined strongly within the sub-wavelength dielectric gap, resulting from the coupling between the SPP waveguide mode and the dielectric waveguide mode. For this reason, the optical mode is called a hybrid mode and, the waveguide which supports this type of modes is called a hybrid plasmonic waveguide (HPW). The physical reason for this hybrid optical mode being confined strongly in the gap is the dominance of the normal components of the electric field at the interfaces of the uncoupled SPP geometry and the dielectric waveguide geometry (nano-wire). Therefore, the requirement of having continuous electric displacement at the material interfaces will result in producing strong normal electric field at the nano-gap. Their study showed a large propagation length between of 40-150 μm and a small effective area ranging from $\lambda^2/400$ to $\lambda^2/40$, where the effective mode area measures the ratio of the total mode energy to the energy density that resides in the core of the waveguide. This propagation length range is good enough for plasmonic device applications because the length of plasmonic devices is aimed to be considerably smaller than that of the current photonic devices in the propagation direction.

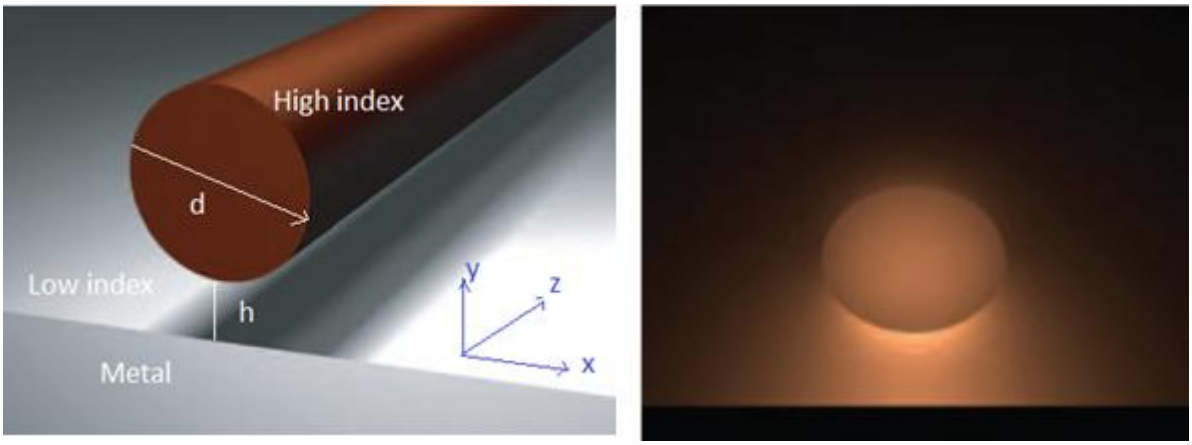


Figure 4: (left) The hybrid plasmonic waveguide geometry, (right) the hybrid optical mode is confined in the sub-wavelength small index gap [35].

On the other hand, using cylindrical hybrid plasmonic waveguides is not practical on integrated photonic chips because of their non-planar fabrication requirements. Therefore, researchers have done much theoretical and experimental research on designing rectangular hybrid plasmonic waveguides to be compatible with silicon-on-insulator (SOI) or complementary metal-oxide-semiconductor (CMOS) technologies. The ability of hybrid plasmonic waveguides to provide low propagation loss and high optical mode confinement motivated researchers to explore HPWs using different geometries and materials [35-41]. Their studies have shown low loss and large propagation distances of several tens of microns, which can permit the use of HPWs in integrated photonic chip technology. In 2011, the first experimental demonstration of a rectangular hybrid plasmonic waveguide at visible and near-infrared optical frequencies was conducted by a research group in Berkeley labs; their experimental results of measuring the propagation length and the confinement strength have agreed with the theoretical simulation results [41]. They have used nano-fabrication methods to fabricate their HPW. HPWs have shown the ability to overcome the diffraction limit with low loss, so they are a good candidate for data routing devices such as modulators and optical switches that will be discussed thoroughly in the following chapter, and for building nano-sized lasers [42].

Chapter 4
Nonlinear All-Optical Switching

Electronic signal processing devices perform logic operations nonlinearly by using electronic elements such as transistors. On the other hand, there is a great demand for all optical devices where the logic operations such as routing, switching, and modulating data are performed optically in order to produce all-optical modern computers. In brief, there is a need for optical transistors. All-optical logic "switching" devices require controlling light with light [43]. This chapter consists of three sections. The first section defines the optical switch, and the second section discusses the significance of nonlinear optical switching. Different geometries of optical waveguides based on the nonlinear phenomenon known as the Kerr effect are presented in the third section.

4.1 Optical Switches

An optical switch is a device that acts as an on/off switch for transmitting optical signals from one element to another one in an optical system. Various optical switching technologies exist. Opto-mechanical switches are one of the early optical switching techniques, where allowing or disallowing optical signal transmission depends on the mechanical movement between optical elements [44**]**. These techniques have many advantages such as low cost, low insertion loss, and low cross- talk, but they have a long switching time (on the order of milliseconds), which limits their use in many applications. The new types of opto-mechanical switches use micro-electro-mechanical systems (MEMS) technology [44-45]. This technology uses mechanical movement of micro-reflective surfaces in order to achieve optical switching. Even though MEMS switches have low cost and consume low power, they have low switching speed on the order of microseconds. Another switching type is electro-optic switches; their switching mechanism depends on the ability to alter a material's refractive index. Some devices such as resonators and waveguide directional couplers can work as electro-optic switches [46]. By applying an external electric field source, the refractive index of the device material can be changed so that the

switching of the light signal can be performed. This technique exhibits fast switching time (nanoseconds), but has high insertion loss [44].

The general problem with electro-optic switches is the requirement of optical-electrical-optical conversion in order to process data in the electronic domain rather than in the optical domain. In communications and network systems, data is transmitted in the optical domain; however, routing and processing data occurs in an electrical domain. Then, signal data is converted to optical domain. These optical-electrical-optical conversions lead to the electronic bottleneck issue that faces high-speed signal processing devices. Due to the increased demand for high-speed signal processing in optical telecommunications and network systems, all-optical switching can provide solutions to this problem.

4.2 The Importance of Nonlinear Optical Switching

In all-optical switches, data processing occurs entirely in the optical domain; that is, a "signal" light can be modulated by a "control" light. It is known that light beams cannot interact with one another when they travel in a linear medium. For example, when two beams of light cross each other in vacuum media, they will emerge unchanged. All-optical switching requires nonlinear interactions. Fortunately, since the emergence of the nonlinear optics field in 1961, a year after the invention of the laser, much interest has been paid to nonlinear optical materials, whose refractive indices depend on the intensity of the incident optical beam. Therefore, in the presence of a nonlinear medium, light can control other light [43]. In this work, we will consider the nonlinear phenomenon known as the Kerr effect, wherein the refractive index of the nonlinear material depends linearly on the intensity of the incident field. The significance of all-optical switches is that they are promising elements for high-density optical communication and network systems [43], wherein the electronic bottleneck issue can be avoided such that electronic integrated circuits might be replaced by photonic ones in the future. For these reasons, a lot of research has been conducted to study the nonlinearity of different optical waveguide structures that will be discussed in the following section.

4.3 Nonlinear Optical Waveguides

Devices based on the Kerr effect can implement sub-picosecond optical switching [47]. The phase shift of a propagating mode in such switching devices will be studied in two cases: neglecting absorption loss and including absorption loss; the latter case will be discussed in the next chapter. The phase shift of a propagating mode in a lossless waveguide can be expressed as

$$\Phi = \frac{2\pi nL}{\lambda}, \tag{35}$$

where L is the waveguide length, λ is the wavelength of the propagating optical signal in the waveguide, and n is the material refractive index, which given by

$$n = n_0 + n_2 I. \tag{36}$$

Here, n_0 is the linear part of the refractive index, and n_2 is the second-order nonlinear index coefficient; this is a material property that measures the degree to which the material refractive index n changes with optical guided mode intensity I. Therefore, Eq. (35) can be written as

$$\Phi = \frac{2\pi(n_0+n_2 I)L}{\lambda} = \Phi_L + \Phi_{NL}, \tag{37}$$

where Φ_L and $\Phi_{NL}$are the linear and nonlinear phase shift of the propagating mode in a lossless waveguide, respectively. Since all-optical switching is a nonlinear process, we are interested in studying the nonlinear phase shift of the propagating optical signal Φ_{NL} in lossless switching devices, which is given by

$$\Phi_{NL} = \frac{2\pi n_2 IL}{\lambda}. \tag{38}$$

Many options are available to achieve a high nonlinear phase shift in order to enhance switching process. The wavelength of an optical signal can be decreased, but wavelength is usually predetermined by other physical or material constraints and can not be altered. The second-order nonlinear index n_2 can also be increased to increase the nonlinear phase shift.

Optical materials have a range of second-order nonlinear indices; however, in this work, the material will be chosen from Ref. [48] in order to compare our results with that work because the authors achieved in their work the highest reported Kerr nonlinearity of slot waveguides. The last option is to increase the optical field intensity I; this can be accomplished by increasing the optical power in the guided or by decreasing the mode's cross-section area. In this work, a low optical power is required for on-chip devices. Therefore, decreasing the mode cross-section area can increase the nonlinear phase shift and enhance the switching process.

Many nano-scale optical waveguides have been proposed based on the Kerr effect to study all-optical switching. For example, silicon nanowires have been shown to have high nonlinearity, but they are limited in size due to the diffraction limit [49]. In addition, photonic crystal waveguides have been shown to have high nonlinearity with strong mode confinement [50] but cannot be easily integrated on chips. Nonlinear dielectric slot waveguides, which confine light in a low-index nonlinear region between high index materials based on the discontinuity of normal electric field components at the interface, have shown a remarkable ability for all optical Kerr switching devices because the light can be confined beyond the diffraction limit in a direction perpendicular to the slot [48]. On the other hand, the degree of the mode confinement is not strongly maximized because parts of the confined optical mode extend out of the outer boundaries of the slot waveguide. Recent studies have shown the potential uses of plasmonic waveguides in Kerr switching systems, where the nonlinear medium is the dielectric material. As mentioned in the previous chapter, plasmonic waveguides can confine light within sub-wavelength structures beyond the diffraction limit. The localization of the SPP optical fields at the metal-dielectric interface means that the electric field amplitude is maximized at the interface; this strong confinement of the field enhances the nonlinear optical effects that depend on the intensity of the optical field. Consequently, this field enhancement in plasmonic waveguides has motivated researchers to study the Kerr nonlinearity in different plasmonic waveguide geometries such as single metal-dielectric interfaces [51] and slab metal-dielectric-metal

structures [52-53]. Fast optical switching speed has been achieved in nano-switching devices, such as ring resonators, by using nonlinear MIM plasmonic waveguides [47, 54-55]. This potential application of plasmonic waveguides is important for the future of all-optical information processing devices in optical integrated circuits. Even though the optical confinement of plasmonic waveguides is very strong at sub-wavelength scales, the propagation loss is very high due to the Ohmic loss of metals, so the propagation length is very short — approximately a few microns. This trade-off between the optical mode confinement and the propagation loss has delayed using plasmonic waveguides in practical applications.

However, hybrid plasmonic waveguides, the recently proposed structures that were discussed in the previous chapter, offer a good balance between mode confinement and propagation loss because they combine the strong confinement of plasmonic waveguides beyond diffraction limit and the long propagation length of dielectric slot waveguides. This advantage of HPWs makes them promising candidates for compact nonlinear devices that require a high degree of optical intensity with low power consumption and high switching speed. Recent research has been conducted to investigate the use of HPWs for nonlinear applications [56-61]. In this work, we are going to model a nonlinear hybrid plasmonic waveguide (NLHPW), study its Kerr nonlinearity, and model a ring resonator device based on the NLHPW.

Chapter 5
Methodology and Analysis

Complex electromagnetic (EM) problems such as waveguide mode solving and propagation often can not be solved analytically due to the complexity of their structures and the applied boundary conditions. For example, when designing a device with complex geometries and mixed boundary conditions, there is a need for other methods that can handle such problems. Computational methods are developed to study complex problems with high precision, in particular, the finite difference method (FDM), the finite element method (FEM), and the beam propagation method (BPM) [62]. One of the most important and commonly-used numerical methods is the finite element method (FEM). Many commercial software packages use this numerical method for practical applications because it can solve very complex problems in different fields such as electricity, electromagnetism, chemistry, and fluid mechanics. In this work, the commercial software COMSOL Multiphysics based on the FEM will be used [63]. This chapter consists of three main sections. The first section will briefly explain the concept of the numerical method FEM; next, the second section will discuss our proposed nonlinear hybrid plasmonic waveguide structure, the method of analyzing the waveguide, and the important results. Finally, the third section will discuss the modeling and method of analysis of a nonlinear ring resonator device based on the NLHPW.

5.1 Finite Element Method

The finite element method uses Maxwell's partial differential equations (PDEs) to solve physical problems; the basic principle of this method depends mainly on four steps [62]. The first step is discretizing a physical object or a solution domain into thousands of small shapes called mesh elements. These finite elements can be defined as one, two, or three dimensional, depending on the study domain of the physical object. Furthermore, the mesh can be generated uniformly or nonuniformly. When there are important regions in the solution domain where the required parameter from studying this physical problem

changes rapidly, it is preferable to define a nonuniform mesh; that is, many of the small elements are concentrated in these regions more than in other regions of the solution domain. The second step is finding the governing PDEs in each element of the mesh. The third step is assembling of all finite elements in the solution domain. Finally, the general solution of the physical problem results from solving all the equations under certain boundary conditions. This computational method is used in many types of waveguide design software to determine EM field profiles and to calculate the guided modes of the waveguide models by using Maxwell's equations. In this work, COMSOL Multiphysics software is used to design a hybrid plasmonic waveguide model and find its guided modes by using the Mode-Eigenvalue solver based on the FEM numerical method.

5.2 Nonlinear Hybrid Plasmonic Waveguide

5.2.1 Waveguide Structure

The proposed nonlinear hybrid plasmonic waveguide geometry in this work is shown in Fig. 5. A nonlinear low-index dielectric material with sub-wavelength thickness t is sandwiched between a high-index silicon ridge with width W and height H_S and a thin silver film with thickness H_M on a silica substrate; the whole waveguide is covered with a dielectric material. The structure can also be inverted – with an upper metal ridge and lower silicon slab – obtaining comparable results. However, we want to keep the proposed arrangement to prevent the creation of plasmonic "hot spots", the concentration of the EM field at the metal corners, which results from the pattering technique of the metallic ridge layer. The materials that are used in designing the waveguide were chosen according to their abundance, their cost, their low optical loss, and their compatibility with current fabrication techniques. For example, silicon and silica are abundant and used in the current integrated circuit technology. Metals such as gold, silver, and aluminum can be used because their plasma resonances are close to the visible light spectrum [64]. In this study, silver is used as the thin metal film because the conductivity of silver is better than gold; therefore, using

gold in waveguides increases the optical loss [40]. Furthermore, the geometry of the hybrid plasmonic waveguides is designed as a rectangular waveguide in order to be compatible with SOI and CMOS technologies.

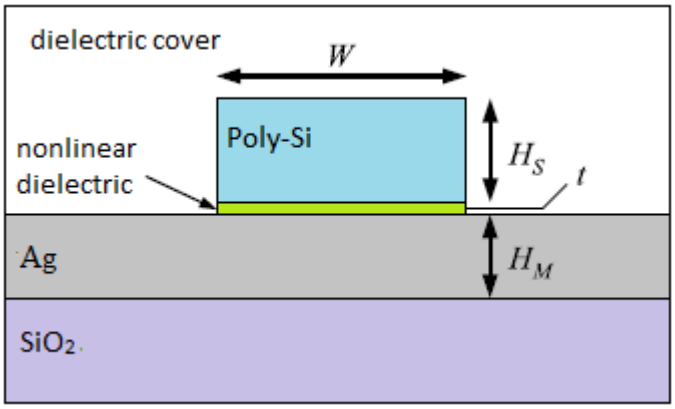


Figure 5 : The proposed geometry of the NLHPW.

5.2.2 Method of Analysis

The trade-off between loss and confinement of plasmonic waveguides represents a barrier to their practical use. Highly-confined plasmonic waveguides tend to have short propagation lengths, that is, the propagating mode attenuates quickly; therefore, the switching of optical signals cannot be achieved. In addition, even though weakly-confined plasmonic waveguides have large propagation lengths, the intensity of the confined mode is too weak; hence, the 2^{nd} order-nonlinear interactions cannot be performed well because strong nonlinear interactions require high optical intensity. Consequently, it is essential to define a figure of merit that maximizes the Kerr nonlinearity of the waveguide in order to optimize the geometry of the nonlinear hybrid plasmonic waveguide. In this work, we will analyze our results in two ways – with and without including linear loss.

5.2.2.1 Without Linear Loss

The effective nonlinearity coefficient γ is a figure of merit that is derived in Ref. 65, based on a full-vectorial nonlinear Schrödinger equation, to calculate the Kerr nonlinearity of waveguides without including propagation loss. It is given by

$$\gamma = \frac{k_0 \bar{n}_2}{A_{\text{eff}}}, \tag{39}$$

where

$$\bar{n}_2 = \frac{\varepsilon_0}{\mu_0} \frac{\iint n_0^2(x,y) n_2(x,y) \left[2\left|\vec{\mathrm{E}}\right|^4 + \left|\vec{\mathrm{E}}^2\right|^2 \right] \mathrm{d}A}{3 \iint \left| (\vec{\mathrm{E}} \times \vec{\mathrm{H}}^*) \cdot \hat{z} \right|^2 \mathrm{d}A}, \tag{40}$$

and

$$A_{\text{eff}} = \frac{\left| \iint (\vec{\mathrm{E}} \times \vec{\mathrm{H}}^*) \cdot \hat{z} \, \mathrm{d}A \right|^2}{\iint \left| (\vec{\mathrm{E}} \times \vec{\mathrm{H}}^*) \cdot \hat{z} \right|^2 \mathrm{d}A}. \tag{41}$$

The effective nonlinear index coefficient $\bar{n}_2$ measures the degree of nonlinear interactions between the nonlinear material and the vector components of the propagating modes, so it involves all the nonlinear characteristic information. The effective mode area A_{eff} represents the ratio of the total mode energy to the energy density of the propagating mode in the waveguide core. The authors developed a generalized vectorial-based relation for the Kerr nonlinear coefficient, which acknowledges that the longitudinal field component E_z of the waveguide mode contributes to the nonlinear processes, resulting in increasing γ more than the scalar-based definition of the Kerr nonlinear coefficient. Maximizing the Kerr nonlinear coefficient requires small effective mode areas that can be achieved by using small cross-section area waveguides. Thus, hybrid plasmonic waveguides that confined modes in sub-wavelength areas can increase the Kerr nonlinearity of the device so that the Kerr-switching process can be successfully achieved. To the best of our knowledge, the highest reported Kerr nonlinear coefficient γ for a lossless slot waveguide structure is $\sim 2 \times 10^4$ $\mathrm{W^{-1}m^{-1}}$ [48].

5.2.2.2 With Linear Loss

It is essential to define a new figure of merit to measure quantitatively the ability of lossy waveguides to provide a nonlinear phase shift Φ_{NL} in order to achieve Kerr nonlinear switching. The intensity of a propagating mode of a lossy waveguide decays exponentially during the propagation, which can be written as

$$I(z) = I_0 e^{-\alpha z}, \tag{42}$$

where the loss coefficient is

$$\alpha = 2k_0 \mathrm{Im}(n_{\mathrm{eff}}). \tag{43}$$

Then, the nonlinear phase shift while propagating over a length L can be written as

$$\Phi_{\mathrm{NL}}(L) = k_0 n_2 \int_0^L I(z)dz = \frac{k_0 n_2 I_0}{\alpha}(1 - e^{-\alpha L}). \tag{44}$$

In our work, we are interested in the nonlinear phase shift over one propagation length L_p, where $L_p = \frac{1}{\alpha}$. Therefore, the best figure of merit to use and maximize in order to optimize our waveguide design is

$$F = \gamma L_p, \tag{45}$$

which can be measured in units of (μm/W·m).

To the best of our knowledge, the highest reported values of Kerr nonlinear coefficient γ for hybrid plasmonic waveguides were disclosed by two groups: the first group achieved $\gamma = 4.1 \times 10^4$ ($W^{-1}m^{-1}$), where the waveguide structure is an elliptical nano-shell, which is shown in Fig. 6(a) [58]. It consists of a nonlinear silicon core, where $n_2 = 1.45 \times 10^{-17}$ m^2/W, coated with a silver shell. This type of the HPWs is not suitable for planar fabrication techniques. In addition, the highest propagation length that is achieved in that work is < 7 μm, leading to $F < 0.1 \times 10^6$ (μm/W·m). The second group achieved $\gamma = 5 \times 10^3$ (W^{-1} m^{-1}), where their waveguide geometry is shown in Fig. 6(b) [60]. It is a rectangular structure, where the nonlinear dielectric layer is an organic polymer DDMEBT with refractive indices of $n_0 = 1.8$ and $n_2 = 1.7 \times 10^{-17}$ m^2/W. The nonlinear dielectric layer is sandwiched

between silver and silicon layer on a silica substrate, and the cover index is air. Their geometry is suitable for planar-fabrication techniques. Furthermore, the highest F value that is achieved in that work is $\sim 0.15 \times 10^6$ (μm/W·m).

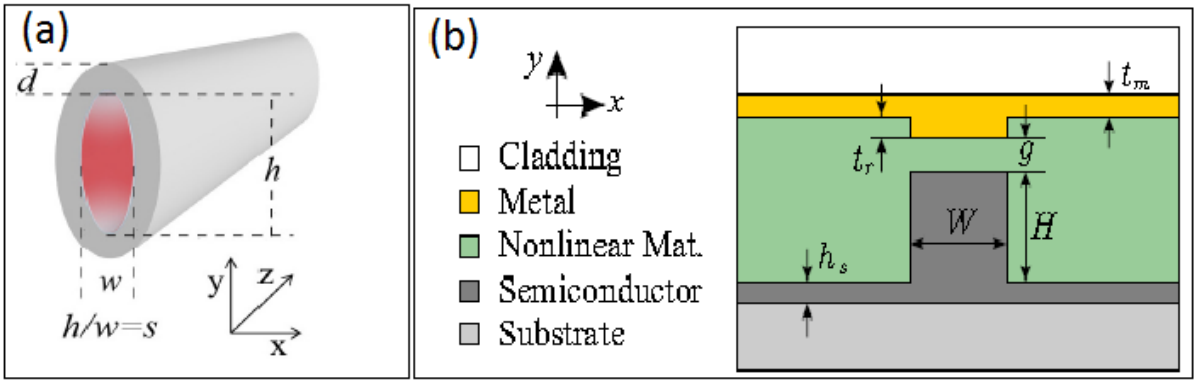


Figure 6: Previous NLHPW geometries: (a) non-planar [58], and (b) planar[60].

5.2.3 Modeling Procedure

COMSOL Multiphysics software is used in order to model our NLHPW and to find the electromagnetic field components of the confined hybrid modes – see Appendix A for detailed information about how we use COMSOL for mode solving simulations. The refractive indices of the NLHPW materials at λ=1550 nm are n_{Si} =3.455, $n_{\mathrm{SiO_2}}$ =1.445, and n_{Ag} =0.1453+11.3587i [66]. The nonlinear dielectric material is an organic material with a high second-order nonlinear refractive index $n_2 \sim 2.2 \times 10^{-16}$ m^2/W and a linear refractive index is n_0=1.7; it is called Poly (p-toluene sulphonate) polydiacetylene PTS (PDA). It was chosen to permit direct comparison of our NLHPW with those used in Ref. 48, which uses the same material. The simulation's geometric parameters are $t = 10$ nm and $H_M = 200$ nm, and the other parameters H_S and W will be scanned in order to find an optimized hybrid plasmonic waveguide design with maximum Kerr nonlinearity. The mesh size that is used in designing the HPW is very small; the distribution of mesh elements is controlled by using high resolution, thousands of elements, in narrow regions such as the sub-wavelength nonlinear dielectric region and the surrounding regions because the hybrid mode is

confined in these regions. Hence, higher accuracy is required here to solve variations of Maxwell's wave equations in each element of the mesh. The finite element mode solver is used to calculate the hybrid guided mode by solving the wave equation for the electric field

$$\vec{\nabla} \times \left(\vec{\nabla} \times \vec{\mathrm{E}}\right) - k_0^2 \varepsilon_r \vec{\mathrm{E}} = 0, \tag{46}$$

where ε_r is the relative permittivity of the materials used in the HPW design. It is related to the refractive index by this relation

$$\varepsilon_r = (n - iK)^2, \tag{47}$$

where n and K are the real and imaginary parts of the refractive index of the waveguide materials. The mode solver is run in order to find the mode eigen-values that represent the effective indices of the guided hybrid mode n_{eff}. The effective mode index is a complex function for lossy waveguides. The real part provides information about how much the mode phase changes during propagation through the waveguide, and the imaginary part measures the propagation loss of the waveguide. A very small imaginary part is required in order to decrease the propagation loss of the waveguide. It is known that plasmonic waveguides support TM-like modes such that the electric field component that is dominant is normal to the metal-dielectric interface (E_y). Fig. 7 shows the surface plot and 1D plot, which is a cross-sectional slice down the center of the waveguide, for the field distribution for the electric field y-component of the fundamental mode that is supported by the HPW. The field is highly concentrated in the nonlinear nano-gap region and decays away from the gap region. We can notice that the decay length of the field into the silicon ridge is longer than that into the metal slab. The physical reason behind that is due to the near lossless nature of dielectric material and the lossy nature of metal.

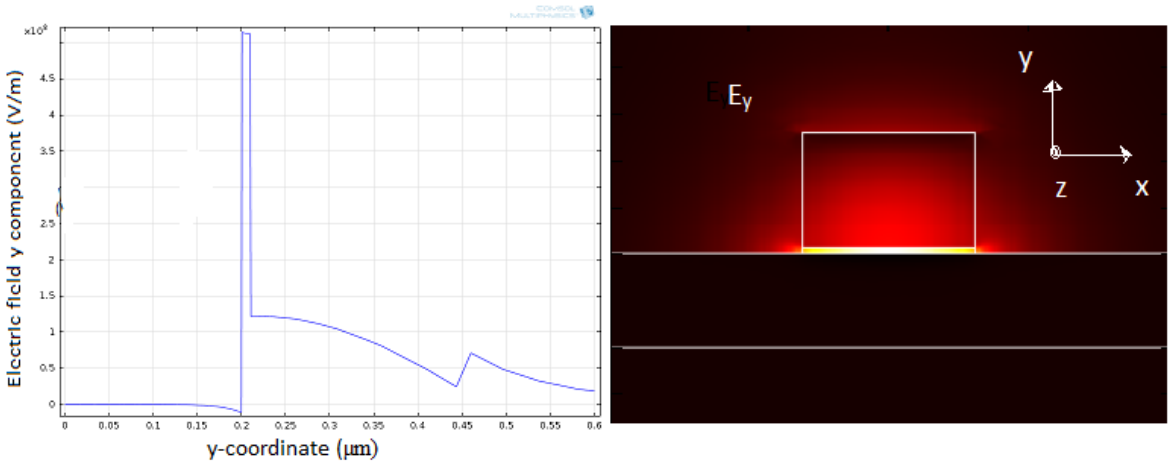


Figure 7: (right) The field distribution for E_y of the hybrid fundamental mode; (left) 1D plot for the $E_y(0,y)$.

5.2.4 Simulation Results

Matlab [67] is also used beside COMSOL software for post-processing, scanning over parameters, and visualizing the results – see Appendix C for a sample of Matlab code used in this work. We first study the effect of the metal film thickness, then the effect of the cover dielectric index. After that, we examine the effect of the silicon ridge height. Finally, we find the optimized values of γ and F by scanning over a wide range of the geometric parameters of the silicon ridge (H_S and W).

5.2.4.1 Effect of the Metal Film Thickness

We scan over a range of the metal film thickness H_M by using the geometric parameters $H_S = W = 250\,\text{nm}$ and $t = 10\,\text{nm}$ and study the effect of the metal thickness on the waveguide performance parameters such as $A_{\text{eff}}, L_p, \bar{n}_2, \gamma$, and F. We find that increasing the metal film thickness approximately has a negligible effect on their values as shown in Fig. 8. For example, the effective mode area of the NLHPW for different metal thicknesses $(100 - 300\,\text{nm})$ is approximately $0.0379\,\mu\text{m}^2$ with negligible variation; this means that, changing the metal film thickness of the NLHPW does not affect the effective area of the hybrid modes. The physical reason behind that is that the hybrid mode is confined at the

interface of the upper portion of the metal film and the sub-wavelength dielectric layer, decaying exponentially into the two materials in a perpendicular direction.

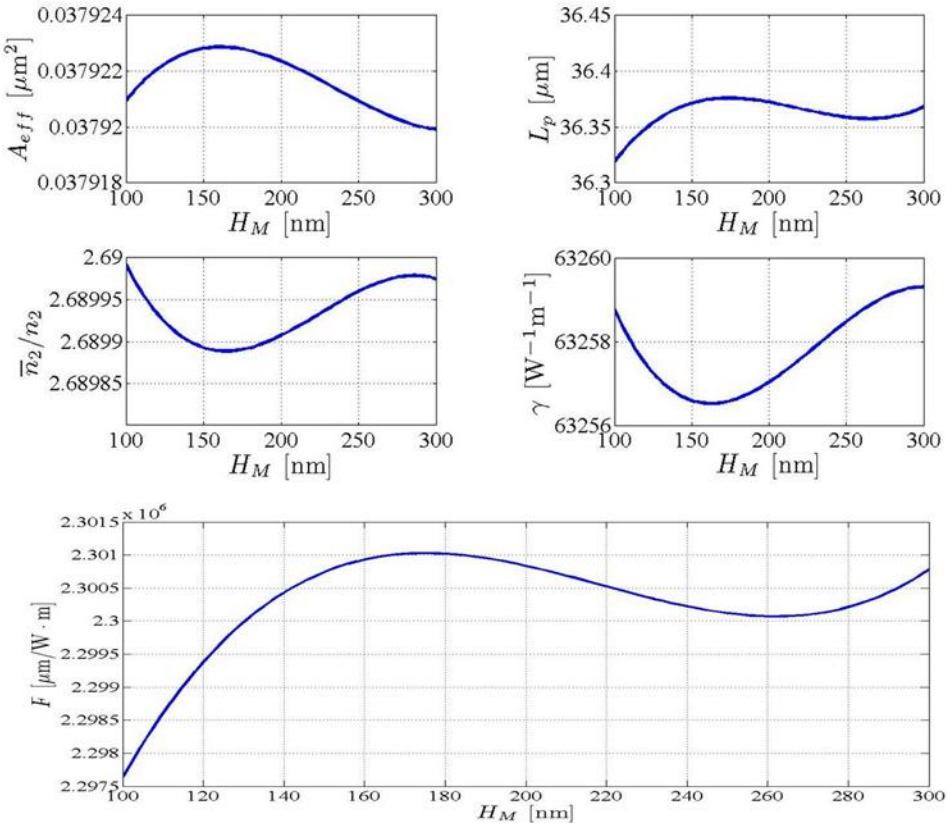


Figure 8: The effect of the metal film thickness on $A_{\text{eff}}, L_p, \bar{n}_2, \gamma$, and F, where the HPW parameters are $H_S = W$= 250 nm, and t=10 nm.

The skin depth δ_m, which is the distance that the EM field can penetrate into the metal, is less than that in dielectric material due to the Ohmic loss of the metal [68]. The skin depth δ_i in the two materials can be measured from the relation

$$\delta_i = (\lambda/2\pi)\sqrt{(\varepsilon_d + \varepsilon_m)/\varepsilon_i^2}. \tag{48}$$

In our case, the skin depth in the metal medium δ_m is approximately 45 nm; therefore, the metal thickness should be higher than the skin depth but not necessary higher than 100 nm since the lower portion of the metal film does not contribute in forming the hybrid mode of

the waveguide. Consequently, the fabrication tolerance of metal film thickness H_M can be increased since changing the metal layer thickness does not affect the waveguide performance as shown in Fig. 8. For the remainder of this work, we will keep the metal film thickness at a constant $H_M = 200$ nm.

5.2.4.2 Effect of the Dielectric Cover Index

Using the geometric parameters $H_S = 250$ nm, $t = 10$ nm, and $H_M = 200$ nm, we scan over a range of the silicon ridge width W and calculate A_{eff}, L_p, $\bar{n}_2$, γ, and F for different dielectric cover indices: air $(n_{\text{air}} = 1)$ and silica $\left(n_{\text{SiO}_2} = 1.445\right)$. Fig. 9 shows the results where the blue line and the black dotted line represent the results for air and SiO_2 cover indices, respectively. When the cover index is reduced, we notice some improvements in the effective mode area A_{eff} that indicate the mode is more highly confined in the transverse direction, and some enhancements in the effective nonlinear index coefficient $\bar{n}_2$ that mean the nonlinear interactions are enhanced in the nonlinear nano-gap. This enhancement in A_{eff} and $\bar{n}_2$ leads to improvements in the values of γ and F. On the other hand, when reducing the cover index, the propagation length decreases. This reduction in the propagation length shows that a large portion of the hybrid mode spreads outward from the nonlinear dielectric nano-gap when the cover index increases. Although this geometric structure is not optimized, it shows that when the cover index is air, we can achieve $\gamma > 8.5 \times 10^4\ \text{W}^{-1}\text{m}^{-1}$, which is 4 times greater than the reported value in the Ref. 48. When the cover index is SiO_2, the maximum value achieved is $\gamma = 6.3 \times 10^4\ \text{W}^{-1}\text{m}^{-1}$, where the width of the silicon ridge $W = 200$ nm. Even though the value of γ and F are reduced with a higher cover index, we will consider the higher dielectric cover index SiO_2 because this layer is important when fabricating devices to prevent oxidation of metals.

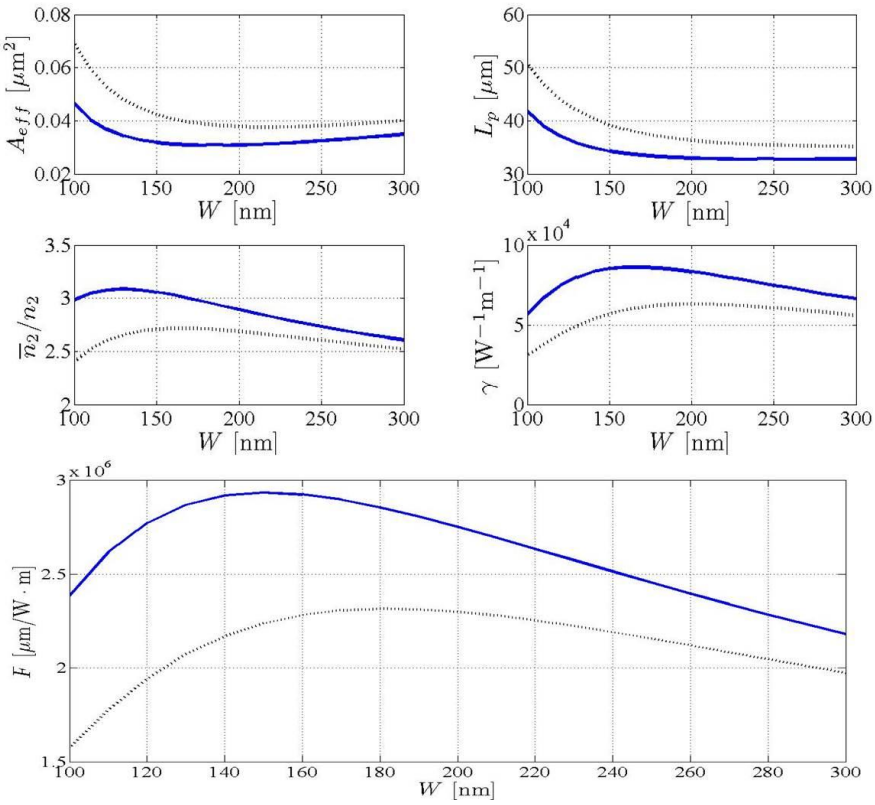


Figure 9: The effect of the cover indices (air,blue) and (SiO2, black dotted) on the A_{eff}, $\bar{n}_2$, γ, and F when the HPW parametres are t= 10 nm, H_S=250 nm, and H_M= 200 nm.

5.2.4.3 Effect of the Silicon Ridge Height

Scanning over a range of the HPW parameter H_S for different values of the nonlinear sub-wavelength gap thickness $t = 10$, 20, 30, 40, and 50 nm is illustrated in Fig. 10. We notice that, when the core thickness decreases, the confinement of the hybrid mode will increase, resulting in enhancement in γ. The variation of the Kerr-nonlinearity is as expected because greater thickness lowers the mode confinement, subsequently lowering the nonlinear response; at the same time, the propagation length increases balancing the decrease of the mode confinement. In addition, we observe that F is only very slightly decreased from $t =$ 10 to 20 nm. This small reduction of F is useful to increase the fabrication tolerance of t.

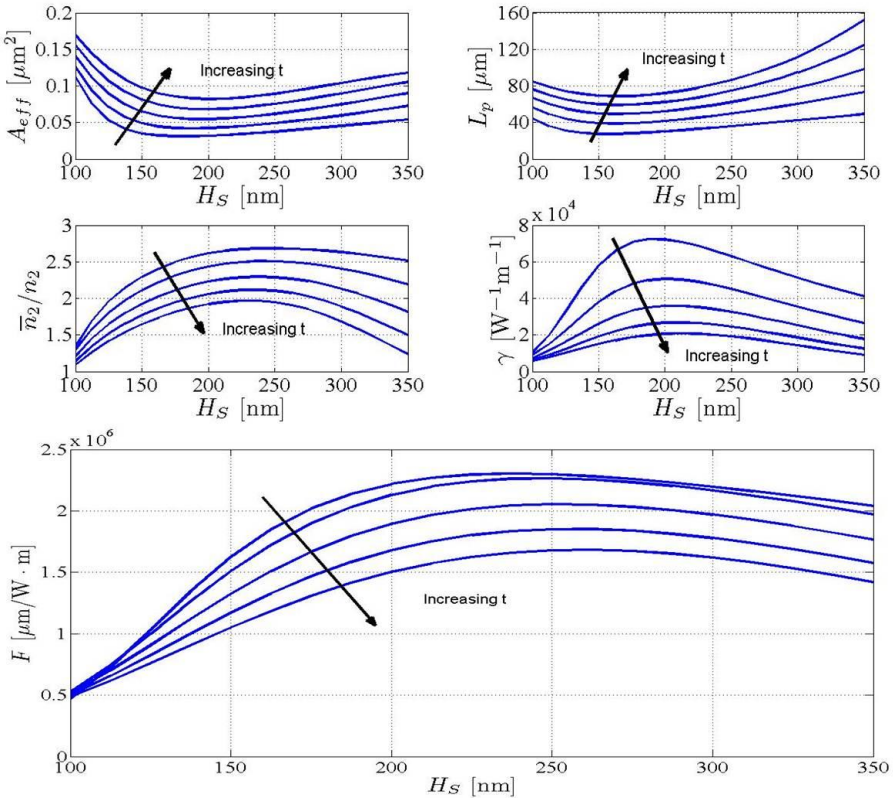


Figure 10: The effect of the ridge height for different values of thickness t=10, 20, 30, 40, and 50 nm on the values of A_{eff}, $\bar{n}_2$, L_p γ, and F.

5.2.4.4 Optimizing Kerr Nonlinearity

Finally, in order to optimize γ and F, two-dimensional scans over a range of the ridge parameters H_S and W are performed, where the core thickness $t = 10$ nm and the metal film thickness is $H_M = 200$ nm; the results are shown in Fig. 11 and Fig. 12. When the HPW parameters are H_S =174 nm and W = 258 nm, a maximum value of $\gamma \sim 7.6 \times 10^4$ W^{-1}m^{-1} can be achieved. This value of γ represents a factor of 2~3 improvement over that which was achieved in the dielectric slot waveguide mentioned in Ref. 48. Furthermore, the maximum value of $F \sim 2.32 \times 10^6$ (μm/W·m) can be achieved when the ridge parameters are H_S = 246 nm and W = 182 nm. This value has improved more than the value achieved in the nano-shell hybrid plasmonic waveguide in Ref. 58 by a factor of ~23. However, because the nonlinear material that is used in our work has a higher n_2 than that used in the

nano-shell HPW work, the improvement in the figure of merit F is actually a factor of ~ 15. In addition, compared to the F value that achieved in the planar hybrid plasmonic waveguide in Ref. 60, our value is improved by a factor ~ 15. Moreover, in their work, they also used the same nonlinear dielectric material that we use in our work, PTS with $n_2 = 2.2 \times 10^{-16}$; they achieved $F \sim 2.5 \times 10^6$, which is slightly higher than our value. However, the cover index of their work is air whereas the cover index in our work is silica which is an important layer when fabricating devices. If we kept air as a cover index, we can achieve $F > 2.9 \times 10^6$. Fig. 11 shows that the innermost contour of F lies at 2.2×10^6, indicating a high tolerance for both H_S and W when fabricating a device.

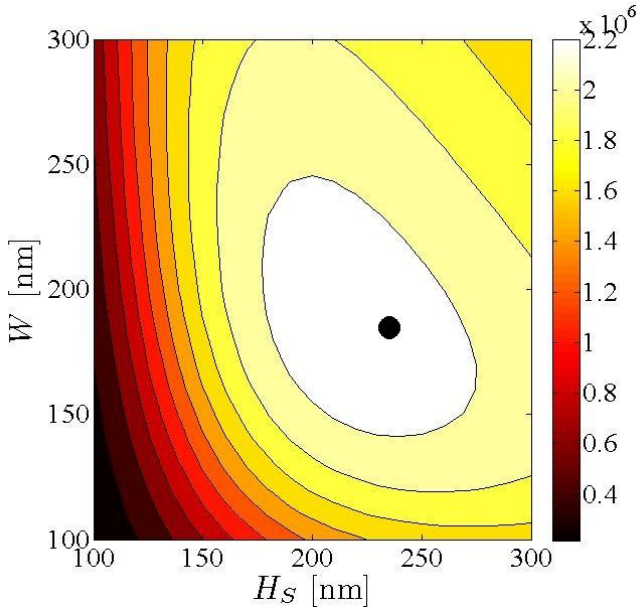


Figure 11: The variation of F with H_S and W, the black dot represents the optimized value of $F = 2.32 \times 10^6$ μm/(W · m) when $H_S = 246$ and $W = 182$ nm.

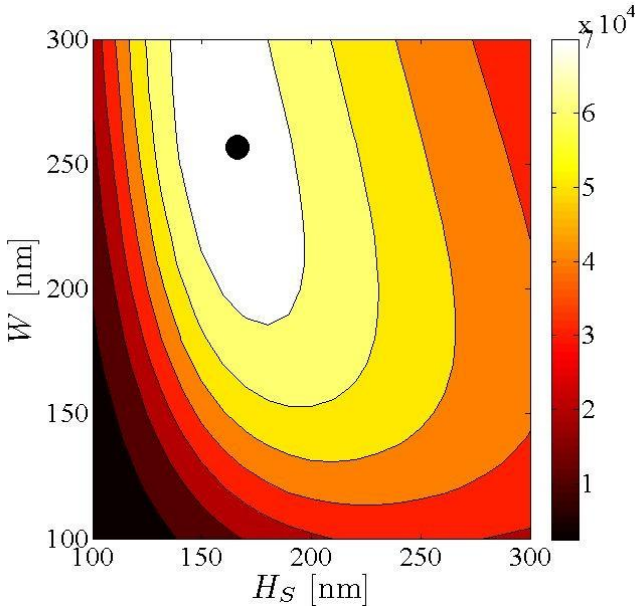


Figure 12: The variation of γ with H_S and W, the black dot shows that the maximum value of $\gamma = 7.64 \times 10^4 (\mathrm{W}^{-1} \cdot \mathrm{m}^{-1})$ is found at $H_S = 174$ and $W = 258$ nm.

5.3 Nonlinear Ring Resonator Device

We propose a resonator-based switch device based on the nonlinear hybrid plasmonic waveguide and study its transmission characteristics numerically by using the frequency-domain simulations. We are currently limited in COMSOL's ability to perform time-domain simulations for nanoscale waveguide devices.

5.3.1 Modeling Procedure

In order to model a three-dimensional ring resonator device based on the NLHPW, we use the Effective Index Method (EIM) to find the effective indices of the NLHPW. The EIM is an approximate analytical method, which involves three steps [69]. The first step is dividing the waveguide structure into different lateral regions; in our case, the regions are shown in Fig. 13. Then, each region can be treated as a slab waveguide, and the effective mode indices of the three regions can be found. It is obvious that the effective indices of the first and the third region are identical, n_1, whereas the effective index of the middle region is different,

n_{II}. The final step is that the effective indices of the three regions can be treated as core and cladding indices in order to find the overall effective index of the whole geometry. We use the eigen mode solver based on the FEM in the COMSOL Multiphysics software in order to find the effective indices of the two slabs of the hybrid plasmonic waveguide. First, we find the effective mode index of the slab hybrid plasmonic wave guide (SHPW), the middle region. For lack of a suitable 1D multilayer slab mode solver, we accomplish this by scanning over an increasing range of the ridge width until the effective mode index of the SHPW stops changing with the width, where the other geometric parameters are kept constant such as H_S =250 nm, H_M =200 nm and t =10 nm. Hence, we find that the effective index of the SHPW is $n_{\mathrm{II}} = n_{\mathrm{effc}} \sim 3.095 + 0.0034i$, which represents the core index of the HPW. Then, we find the effective index of the cladding region of the SHPW by scanning over a range of the metal film width until the effective index of the mode stops changing with the width; we obtain $n_I = n_{\mathrm{effcl}} \sim 1.4579 + 0.000307i$. In addition, the analytical method to find the effective mode index of the SPPs for a single metal-dielectric interface $N_{\mathrm{eff}} = k_{spp}/k_0$ can be used, since – as shown previously – the bottom surface of the metal layer has negligible effect on the SPP mode. This results in the same effective index of the cladding regions. Consequently, the effective mode indices of the core and cladding regions are used to find the mode effective index of the whole geometry by modeling a slab waveguide with the new indices n_{effc} and n_{effcl}.

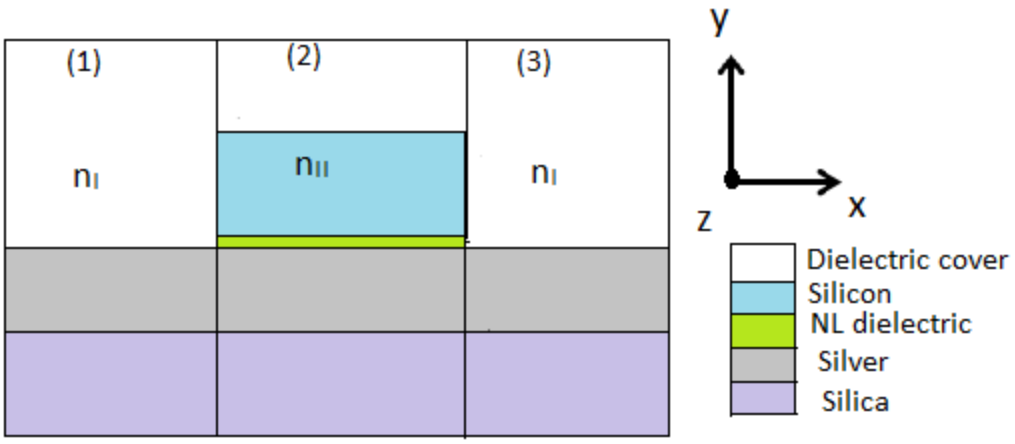


Figure 13: A schematic diagram of the effective index method applied on the NLHPW.

In order to launch an input power into the slab waveguide and study the transmission of the propagating mode in the frequency domain, two study steps are required: the boundary mode analysis and the frequency domain. In the first study step, COMSOL software finds the solutions for the mode at the two ports in the boundaries of the waveguide. Then, the frequency domain is linked to the results of the boundary mode analyses. Fig. 14 illustrates a 2D plot of the z-component of the electric field in the waveguide, where the core width is $200\ \mathrm{nm}$. There is a change in axes: what was "y" in 2D mode solving is "z" for frequency-domain simulation. In addition, the 1D plot for the power propagating in the x-direction shows a propagation length of approximately 38 μm (Fig. 15), as expected from the imaginary part of the core mode index. Finally, a resonator is added next to the straight waveguide using the same effective indices in order to model a 2D resonator-based all optical switching device based on the NLHPW, which will be discussed in the next section – see Appendix B for a report about how we use COMSOL software to perform frequency domain simulation of the nonlinear ring resonator device.

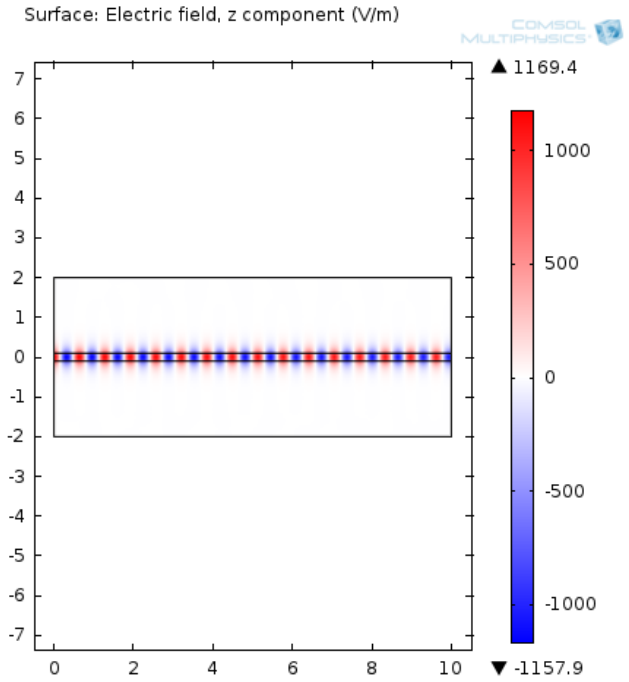


Figure 14: A 2D plot for the electric field E_z in the waveguide, where the *x* and *y* axes represent the computational domain of the waveguide in microns.

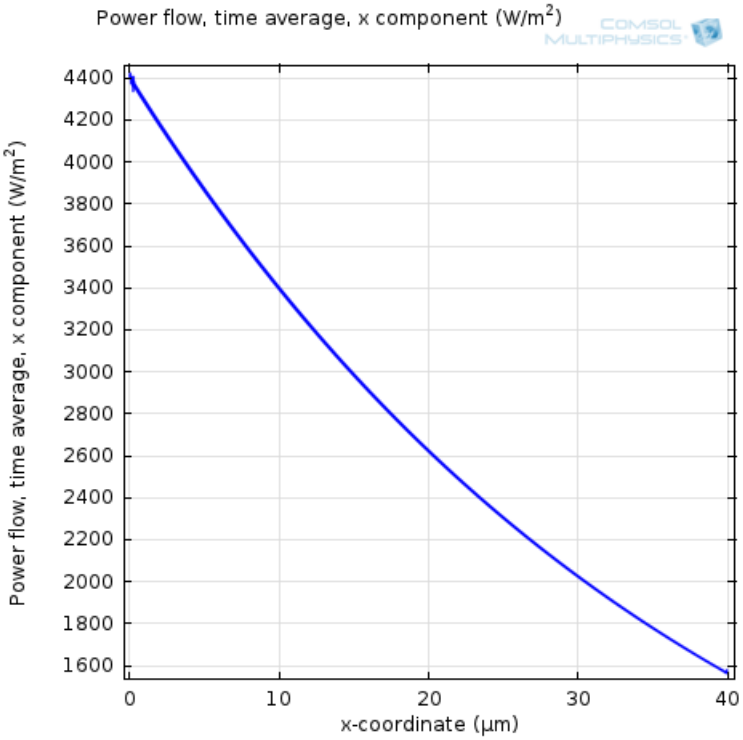


Figure 15: A 1D plot for the power flow in the x-direction of the waveguide.

5.3.2 Device Analysis

A simple structure of a ring resonator device based on the NLHPW is shown in Fig. 16, where W_c is the core width, r is the ring radius, and d is the separation distance between the waveguide and the ring. If we input a signal of SPP modes into the straight waveguide (SWG), some of the modes will be coupled into the resonator and will experience multiple passes around; then, this signal will interfere with the remaining SPP signal, constructively or destructively, depending on the ring circumference and its effective index, which can have a nonlinear shift. We are interested in studying the transmission characteristics of the device, which can be described by the relation

$$T = \left|\frac{B}{A}\right|^2 = \frac{|t_c|^2+|\alpha_l|^2-2\alpha_l|t_c|\cos(\theta)}{1+|\alpha_l t_c|^2-2\alpha_l|t_c|\cos(\theta)}. \quad (49)$$

Here, T is the intensity of the transmitted field at the output of the SWG; A and B are the amplitude of the transmitted fields at the input and the output of the SWG; t_c is the coupling factor between the SWG and the ring; α_l is the loss factor in the ring; and θ $(= 2\pi L n_{\text{effc}} / \lambda)$is the phase shift per circulation in the ring; $L\,(= 2\pi r)$ is the ring circumference; and n_{effc} is the effective index of the ring [70]. The resonance condition occurs at

$$\theta = 2m\pi, \text{ or at } Ln_{\text{effc}} = m\lambda, \quad (50)$$

where m is an integer. We are interested in achieving critical coupling, where the coupling factor should match the loss in the ring so that the transmission drops down to the minimum value at the resonance. The loss in the ring $\alpha_l\left(= e^{-\alpha_r L/2}\right)$ is related to the geometric parameters in the ring, where α_r is the intensity absorption coefficient in the ring. Some factors have an effect on implementing an optimum coupling factor that helps show sharp resonances such as the ring radius r and the separation distance between the SWG and the ring in the coupling region d. The performance of ring resonators can be

measured by finding the free spectral range (FSR), and the full width at half maximum (FWHM) from the transmission spectrum [71]. The free spectral range (FSR) is the wavelength or frequency distance between two transmission dips or resonance peaks, which can be given as

$$\mathrm{FSR} = \Delta\lambda \approx \frac{\lambda^2}{n_{\mathrm{effc}} L}. \tag{51}$$

It is related to the resonator geometric parameter, the ring length L, and the effective mode index of the resonator n_{effc}. The FWHM $\Delta\lambda_{\mathrm{FWHM}}$ is the width of the resonance peak where the power drops to half its value at the resonance wavelength.

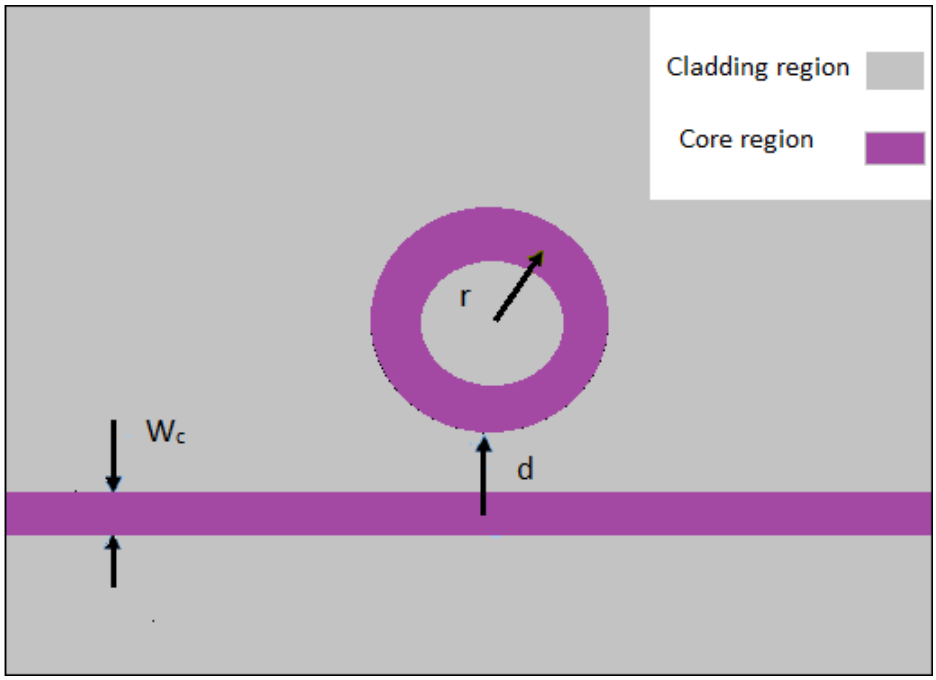


Figure 16: A schematic diagram of the nonlinear ring resonator device.

5.3.3 Results and Discussion

We use COMSOL software to adjust the geometric parameters of the ring resonator device such as $W_c = 200\ \mathrm{nm}$, $d = 250\ \mathrm{nm}$, and $r = 1\ \mu\mathrm{m}$, and do a single frequency domain

simulation at $\lambda = 1550\ \mathrm{nm}$ by launching a input power $1\ \mathrm{mW}$. We find that the resonance condition is satisfied at $\sim 1.55\ \mu\mathrm{m}$, and the field intensity inside the ring is enhanced 4 times higher than the intensity in the input waveguide as shown in Fig. 17. This enhancement of the field intensity in the ring resonator makes it a candidate for nonlinear optical applications, which require a high optical field intensity to perform nonlinear interactions, such as optical switching devices. We scan over a range of wavelengths in order to find the transmission spectrum of the resonator in dB units, $T_{\mathrm{dB}} = 10\log_{10}(T)$. Fig. 18 shows the transmission spectrum of the resonator; it illustrates how the nonlinear ring resonator permits transmission a range of wavelength through the output of the waveguide except at two wavelengths, which satisfy the resonance conditions in the ring; the two sharp resonance peaks are at $1.46\ \mu\mathrm{m}$ and 1.55 μm with transmission approximately -14 and $-20\ \mathrm{dB}$, respectively. The spacing in wavelength between the two resonances is ~ 90 nm, which approximately agrees with Eq. (49). We are interested in the sharp resonance at $1.55\ \mu\mathrm{m}$; it has low transmission $\sim 0.01\ (\sim -20\ \mathrm{dB})$ with a FWHM $\sim 9\ \mathrm{nm}$, where the power drops $3\ \mathrm{dB}$ of its initial value. We notice that the transmission spectrum does not start from zero dB; this is due to the propagation loss of the waveguides. The propagation loss per unit length $\alpha_{\mathrm{loss}}\ (\mathrm{dB}/\mu\mathrm{m})$ can be calculated as: $\alpha_{\mathrm{loss}} = \frac{1}{L_p} \times 10\log_{10}(T)$, where $L_p = \frac{1}{2\ Im[n_{\mathrm{effc}}]k_0}$ and $T = 1/e$. The propagation length of the input waveguide is $\sim 38\ \mu\mathrm{m}$, so the propagation loss per unit length is $\sim 0.12\ \mathrm{dB}/\mu\mathrm{m}$. Furthermore, there is loss in the ring $\sim 0.1\ \mathrm{dB}/\mu\mathrm{m}$, and the bending loss does not seem high with 1 micron radius.

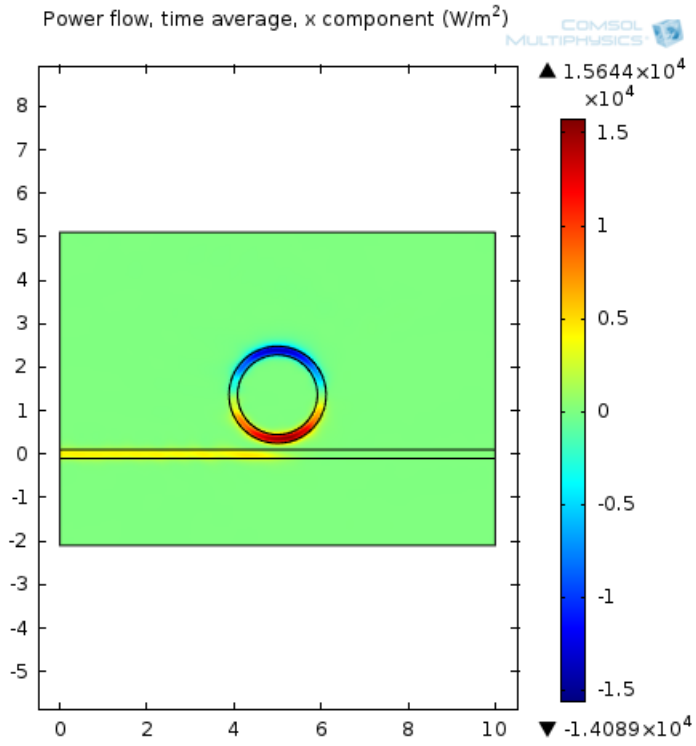


Figure 17: A surface plot shows the power flow in the *x*-direction of the ring resonator device at the resonance, where the intensity in the ring is enhanced 4 times more than the input waveguide, the horizontal and vertical axes represent the computational domain in microns.

The power of the input signal can affect transmission of the device, resulting in a nonlinear resonance shift. For example, if we input a power $P = 300$ mW into the input waveguide, where the effective mode area of our NLHPW is approximately $A_{\text{eff}} = 0.05\ \mu\text{m}^2$, the signal intensity will be $I = 6 \times 10^{12}\ \text{W/m}^2$. Changing the data signal intensity will lead to change the core index of the input waveguide by $\Delta n = n_2 I = 0.0013$ and the ring by $\Delta n = n_2(4I) = 0.0053$, where $n_2 = 2.2 \times 10^{-16}\ \text{m}^2/\text{W}$ is the 2^{nd} order nonlinear refractive index of the nonlinear dielectric material, which depends on the intensity of the field. The change in the ring core index is more than that of input waveguide because of the enhancement of the transmitted field in the ring more than in the input waveguide by a factor ~ 4. This nonlinear index shift in the core indices will affect the critical coupling between the waveguide and the ring so that the resonance peak and its transmission will be shifted. Fig. 19 shows the nonlinear resonance shift of the resonance peak and its

transmission for different input power *P*=300, 400, and 500 mW. We notice that a few 100 mW of optical power, which is considered high power for devices on chips, is required in order to switch the beam more than half the FWHM of the device resonance peak which is at *P*=1 mW. In practical case, when we build a device on a chip, a few mW of optical power is required in order to operate it. These high input powers is not a problem for us because for optical switching we would use short pulsed laser, and we can switch beam in short duty cycle. That means the required *average* power to switch data is much lower than the actual switching beam power (peak power) by two or three orders of magnitude.

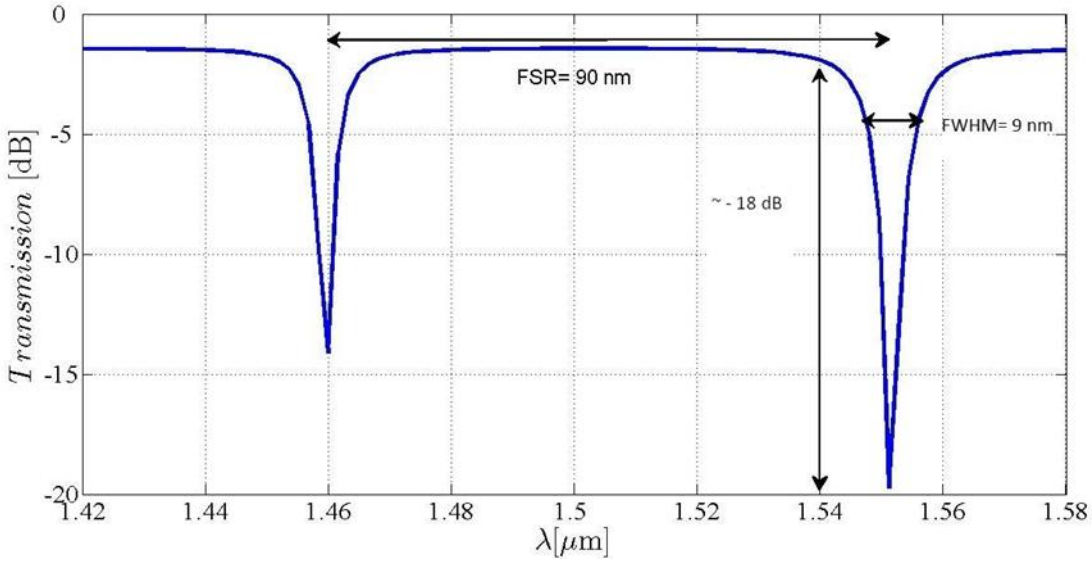


Figure 18: The transmission spectrum of the nonlinear ring resonator device; it shows the FSR, FWJM, and the depth of the resonance peak at ~ 1.55 μm.

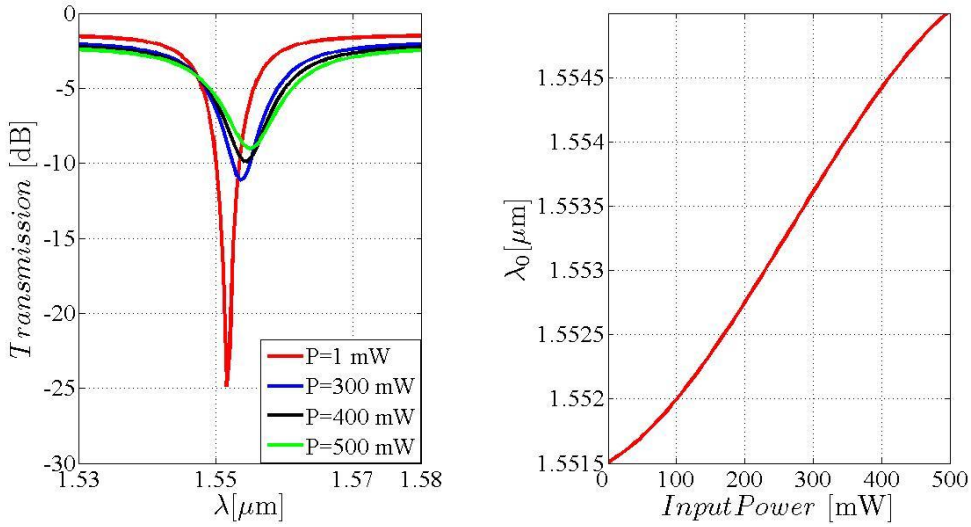


Figure 19: (left) The nonlinear resonance shift of the ring resonator transmission for different input powers; (right) the shift in nonlinear resonance wavelengths increase as input power increases.

Chapter 6
Conclusion and Future Steps

Surface plasmon polariton (SPP) based devices have received much attention in recent years in different applications such as biosensing and waveguiding. The ability of plasmonic waveguides to confine light into nanoscale structures well beyond the diffraction limit has motivated researchers to propose different geometries and structures in order to address the high propagation loss of these waveguides. One of the recent proposed plasmonic waveguide structures is the hybrid plasmonic waveguide that has shown a good balance between mode confinement and propagation loss. The main goal of this thesis was to design a nonlinear hybrid plasmonic waveguide (NLHPW), to study its nonlinear optical performance based on the Kerr effect, and to investigate its uses in nonlinear optical applications such as a nonlinear optical switch device.

In Chapter 2, the advantages and disadvantages of both metallic wire interconnects and conventional photonic interconnects were discussed, and how plasmonic interconnects could exploit and combine their advantages were introduced in Chapter 3. Moreover, the underlying physics of SPP modes was analyzed theoretically by using Maxwell's wave equations, and the dispersion relation was derived. Then, different types of plasmonic waveguides were discussed and it was determined that hybrid plasmonic waveguide structures could balance between loss and confinement.

In Chapter 4, optical switches and how nonlinear optical switching is significant for data processing in optical communication systems were explained. Furthermore, different types of nonlinear optical waveguides based on the Kerr effect were discussed and how nonlinear hybrid plasmonic waveguides are good candidates for nonlinear applications.

In Chapter 5, the Finite Element Method was explained, which is a numerical analysis for waveguide mode solving problems. By using COMSOL Multiphysics software based on the FEM, the nonlinear hybrid plasmonic waveguide was modeled, and its guided modes were found. The nonlinear optical performance of the NLHPW was measured by

using appropriate figure of merits such as Kerr nonlinear coefficient γ without including loss and F with including loss. Our proposed optimized NLHPW geometry has been shown high Kerr nonlinear coefficients $\gamma = 7.64 \times 10^4\ \mathrm{W^{-1}m^{-1}}$ and $F = 2.32 \times 10^6\ \mu\mathrm{m/W \cdot m}$ compared to the other proposed NLHPWs. Moreover, a nonlinear ring resonator device based on the NLHPW was modeled and analyzed theoretically. The enhancement of the field intensity in the ring was four times higher than the field intensity in the input waveguide. In addition, the effect of using different input power on the signal transmission resulted in a nonlinear resonance shift of the resonance peak.

For future steps, there are some directions to extend the research in this thesis. One way is fabricating the nonlinear hybrid plasmonic waveguide by using nano-fabrication tools and measuring its optical characteristics by using near-field microscopy techniques. Furthermore, the nonlinear dielectric material can be changed with different nonlinear materials and observe their influence on the Kerr nonlinearity of the waveguide. Moreover, the nonlinear ring resonator device can be studied in the time domain by using a simulation based on the Finite Difference Time Domain (FDTD) or Finite Element Time Domain (FETD) Methods, which can help measure the switching speed of the device. In addition, the proposed nonlinear ring resonator can be fabricated and all optical switching effect can be achieved by using two sources of light: the data signal and switching (control) signal. By changing the intensity of switching signal during the propagation of data signal, the nonlinear index of the Kerr material will change, resulting in performing the switching process. Therefore, an ultra-fast all optical switching device based on the NLHPW will have potential use in nanophotonic integrated circuits to process data in the optical domain.

APPENDICES

Appendix A: Mode-Solving Simulation Report

This appendix presents a full report, which generated by using COMSOL software, about the mode-solving simulation steps to calculate the guided eigen-modes of the hybrid plasmonic waveguide used in this work. This report explains the four main steps in order to perform mode-solving simulations. The first step is to define the geometrical parameters of the waveguide and the refractive indices of the materials. Designing the geometry, applying the boundary conditions, and defining the mesh are the second step. Then, the eigen mode solver based on the finite element method is chosen in order to calculate the hybrid modes of the waveguide. Finally, the results such as mode field distribution can be analyzed visualized in different ways such as a 1D plot, which results from a horizontal or vertical cross-sectional slice in the waveguide, or a 2D surface plot.

Contents

1. Global Definitions....51
   1.1. Parameters 1....51
2. Model 1 (mod1)....52
   2.1. Definitions....52
   2.2. Geometry 1....52
   2.3. Materials....54
   2.4. Electromagnetic Waves (emw)....59
   2.5. Mesh 1....62
3. Study 1....64
   3.1. Mode Analysis....64
   3.2. Solver Configurations....64
4. Results....66
   4.1. Data Sets....66
   4.2. Tables....66
   4.3. Plot Groups....67

1 Global Definitions

1.1 Parameters 1

Parameters

Name	Expression	Description
W	.200	waveguide width
H	.25	waveguide height
t	.01	NL dielectric thickness
Hm	.2	metal film thickness
Hsio2	.4	silica substrate thickness
xClad	.6	Distance to adjust the domain width
WD	W + 2*xClad	Domain width
HD	Hsio2 + Hm + t + H + .25	Domain height
nSiO2	1.445	Sio2 refractive index
nl	1.7	NL refractive index
nc	1.445	dielectric cover refractive index
nAgR	.1453	Real part of metal refractive index
nAgI	-11.3587	Imaginary part of metal refractive index
nSi	3.455	Silicon refractive index
wl	1.55	free space wavelength
f0	c_const/wl	frequency
nSeed	2.377	initial seed index value to help find the correct mode

2 Model 1 (mod1)

2.1 Definitions

2.1.1 Coordinate Systems

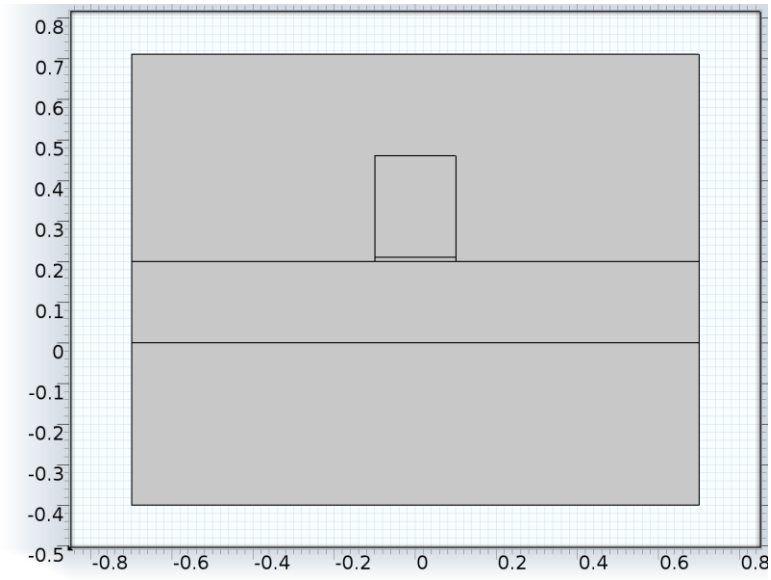
Boundary System 1

Coordinate system type	Boundary system
Identifier	sys1

Settings

Name	Value
Coordinate names	{t1, n, to}
Create first tangent direction from	Global Cartesian

2.2 Geometry 1



Geometry 1

units

Length unit	µm
Angular unit	deg

Geometry statistics

Property	Value
Space dimension	2

Property	Value
Number of domains	5
Number of boundaries	18

2.2.1 Sio2 base (r1)

Position

Name	Value
Position	{0, Hsio2/2}
Base	Center
Width	WD
Height	Hsio2
Size	{WD, Hsio2}

2.2.2 Domain (r2)

Position

Name	Value
Position	{WD/2, Hsio2}
Width	WD
Height	HD
Size	{WD, HD}

2.2.3 silver (r3)

Position

Name	Value
Position	{0, Hm/2}
Base	Center
Width	WD
Height	Hm
Size	{WD, Hm}

2.2.4 NL (r4)

Position

Name	Value
Position	{0, Hm + (t/2)}

Name	Value
Base	Center
Width	W
Height	t
Size	{W, t}

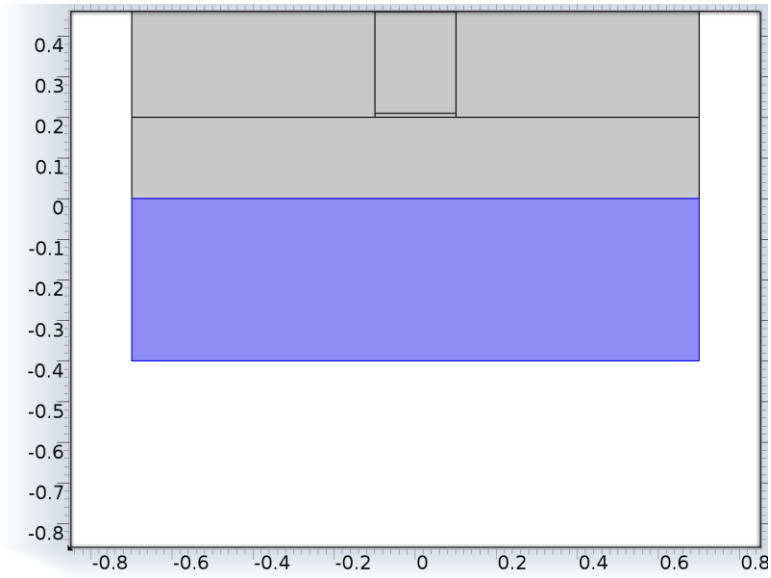
2.2.5 Rectangle 5 (r5)

Position

Name	Value
Position	{0, Hm + t + (H/2)}
Base	Center
Width	W
Height	H
Size	{W, H}

2.3 Materials

2.3.1 sio2 base



Sio2 base

Selection

Geometric entity level	Domain
Selection	Domain 1

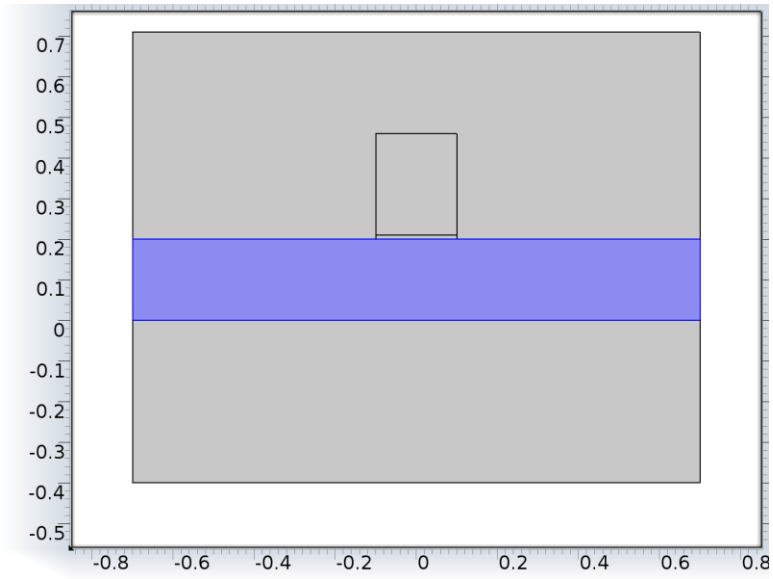
Material parameters

Name	Value	Unit
Refractive index	nSiO2	1
Refractive index, imaginary part	0	1

Refractive index Settings

Description	Value
Refractive index	{{nSiO2, 0, 0}, {0, nSiO2, 0}, {0, 0, nSiO2}}
Refractive index, imaginary part	{{0, 0, 0}, {0, 0, 0}, {0, 0, 0}}

2.3.2 silver



Silver

Selection

Geometric entity level	Domain
Selection	Domain 2

Material parameters

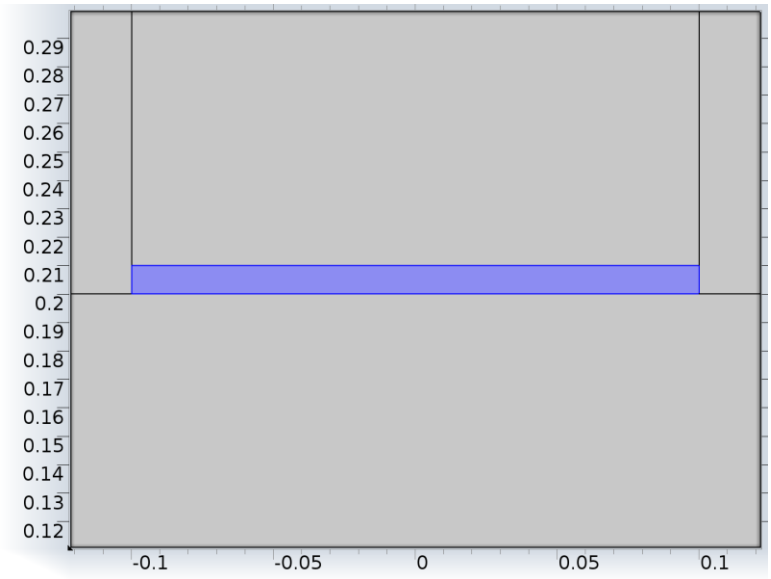
Name	Value	Unit
Refractive index	nAgR	1
Refractive index, imaginary part	nAgI	1

Refractive index Settings

Description	Value

Description	Value
Refractive index	{{nAgR, 0, 0}, {0, nAgR, 0}, {0, 0, nAgR}}
Refractive index, imaginary part	{{nAgI, 0, 0}, {0, nAgI, 0}, {0, 0, nAgI}}

2.3.3 NL



NL

Selection

Geometric entity level	Domain
Selection	Domain 4

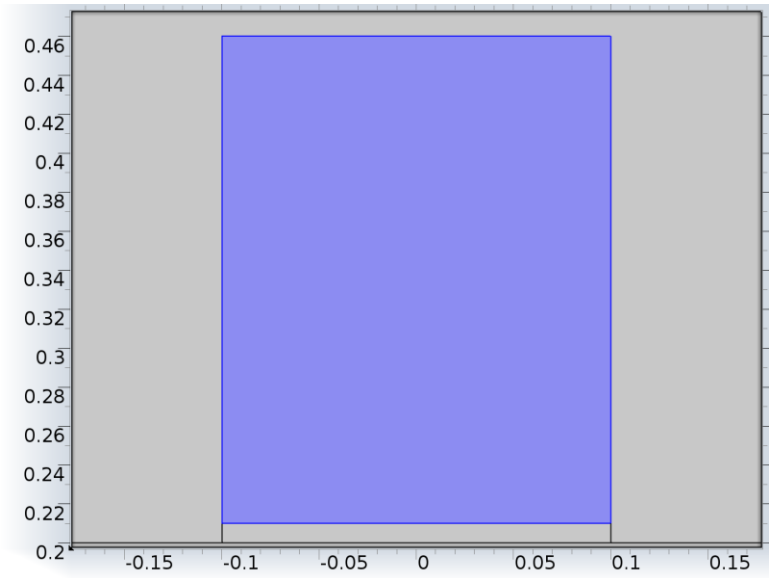
Material parameters

Name	Value	Unit
Refractive index	nl	1
Refractive index, imaginary part	0	1

Refractive index Settings

Description	Value
Refractive index	{{nl, 0, 0}, {0, nl, 0}, {0, 0, nl}}
Refractive index, imaginary part	{{0, 0, 0}, {0, 0, 0}, {0, 0, 0}}

2.3.4 Silicon



Silicon

Selection

Geometric entity level	Domain
Selection	Domain 5

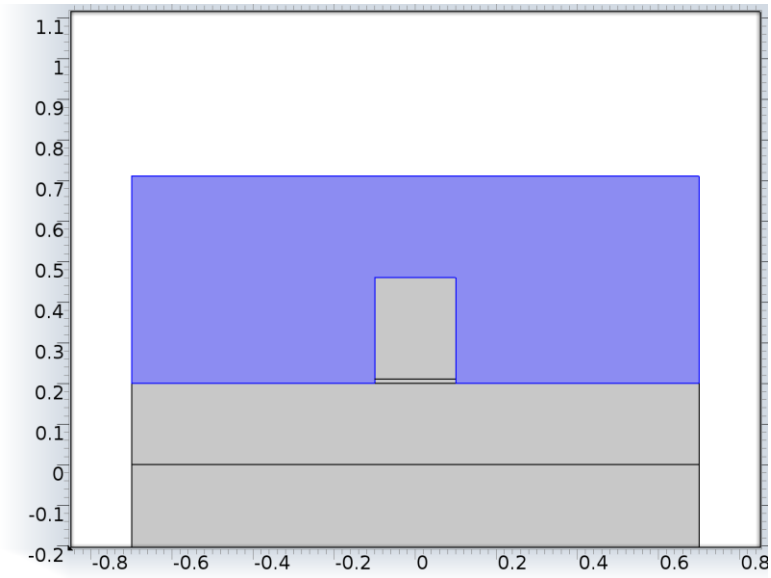
Material parameters

Name	Value	Unit
Refractive index	nSi	1
Refractive index, imaginary part	0	1

Refractive index Settings

Description	Value
Refractive index	{{nSi, 0, 0}, {0, nSi, 0}, {0, 0, nSi}}
Refractive index, imaginary part	{{0, 0, 0}, {0, 0, 0}, {0, 0, 0}}

2.3.5 cover



cover

Selection

Geometric entity level	Domain
Selection	Domain 3

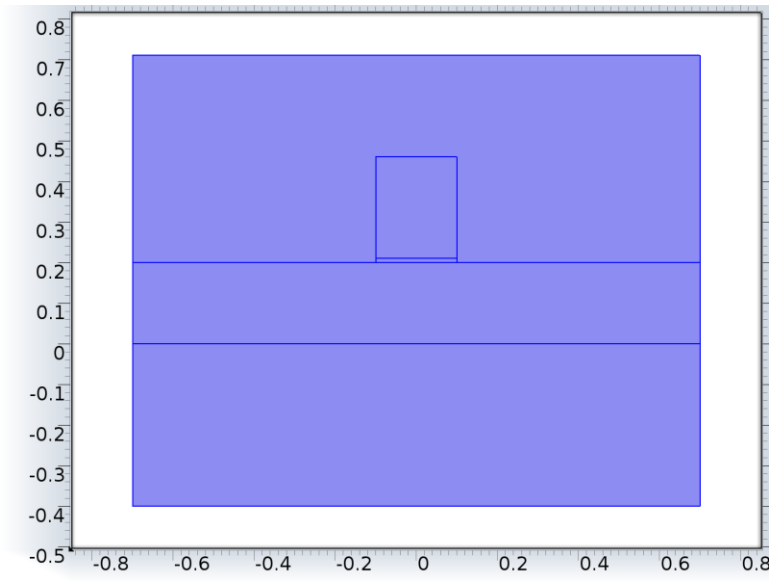
Material parameters

Name	Value	Unit
Refractive index	nc	1
Refractive index, imaginary part	0	1

Refractive index Settings

Description	Value
Refractive index	{{nc, 0, 0}, {0, nc, 0}, {0, 0, nc}}
Refractive index, imaginary part	{{0, 0, 0}, {0, 0, 0}, {0, 0, 0}}

2.4 Electromagnetic Waves (emw)



Electromagnetic Waves

Selection

Geometric entity level	Domain
Selection	Domains 1–5

Equations

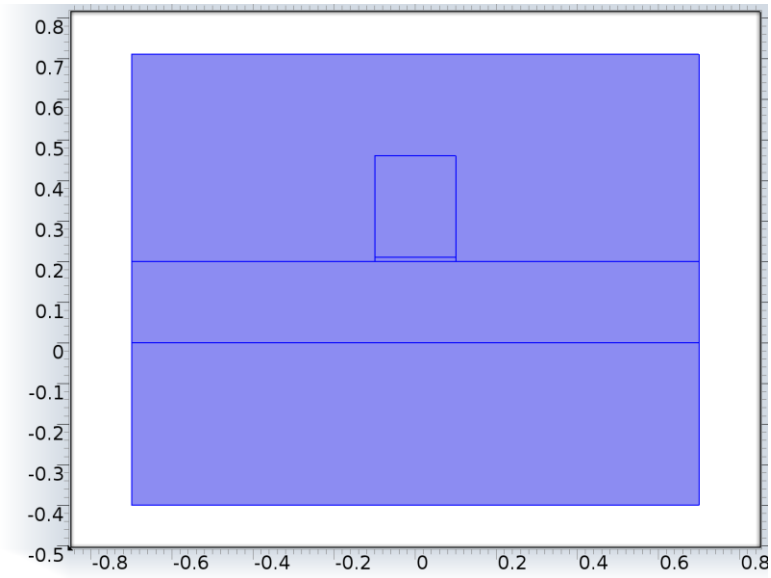
$$\nabla \times \mu_r^{-1}(\nabla \times \mathbf{E}) - k_0^2(\epsilon_r - \frac{j\sigma}{\omega\epsilon_0})\mathbf{E} = \mathbf{0}$$

$$\lambda = -j\beta - \delta_z$$

Settings

Description	**Value**
Show equation assuming	std1/mode

2.4.1 Wave Equation, Electric 1



Wave Equation, Electric 1

Selection

Geometric entity level	Domain
Selection	Domains 1–5

Equations

$$\nabla \times (\nabla \times \mathbf{E}) - k_0^2 \varepsilon_r \mathbf{E} = \mathbf{0}$$

$$\lambda = -j\beta - \delta_z$$

Settings

Settings

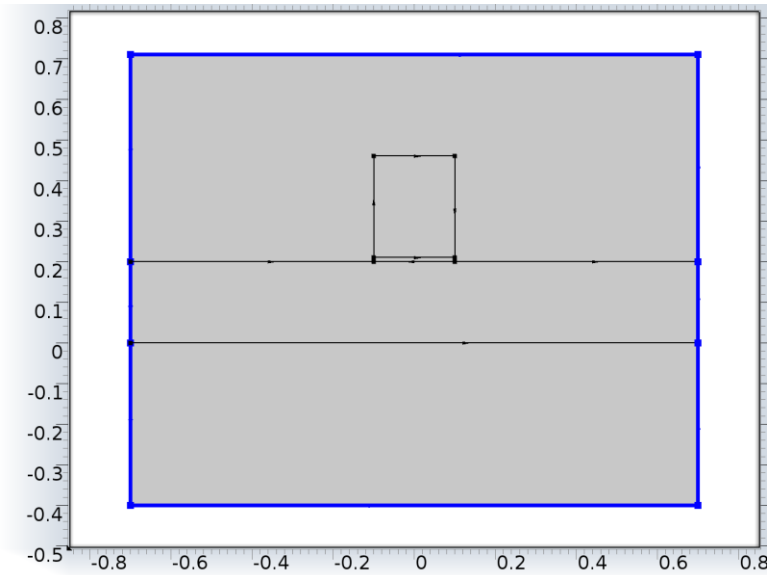
Description	Value
Electric displacement field model	Refractive index

Properties from material

Property	Material	Property group
Refractive index	sio2 base	Refractive index
Refractive index, imaginary part	sio2 base	Refractive index
Refractive index	silver	Refractive index
Refractive index, imaginary part	silver	Refractive index
Refractive index	NL	Refractive index
Refractive index, imaginary part	NL	Refractive index

Property	Material	Property group
Refractive index	Silicon	Refractive index
Refractive index, imaginary part	Silicon	Refractive index
Refractive index	cover	Refractive index
Refractive index, imaginary part	cover	Refractive index

2.4.2 Perfect Electric Conductor 1



Perfect Electric Conductor 1

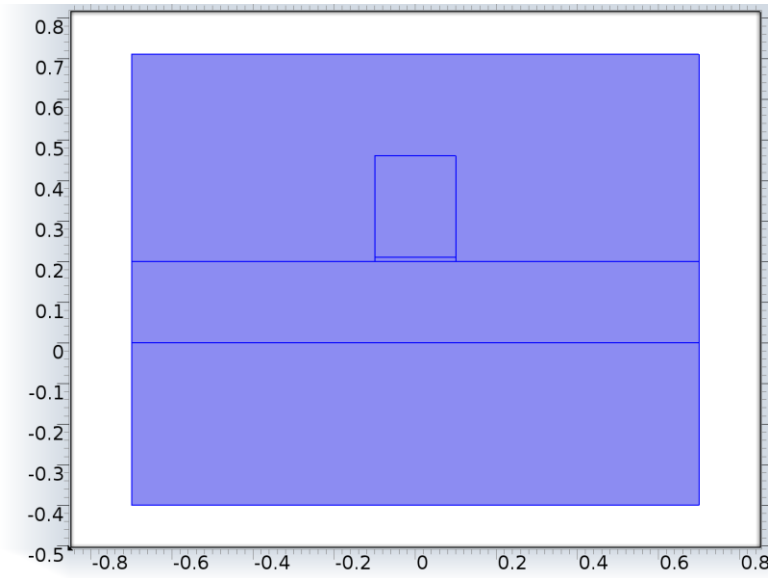
Selection

Geometric entity level	Boundary
Selection	Boundaries 1–3, 5, 7, 16–18

Equations

$$\mathbf{n} \times \mathbf{E} = 0$$

2.4.3 Initial Values 1

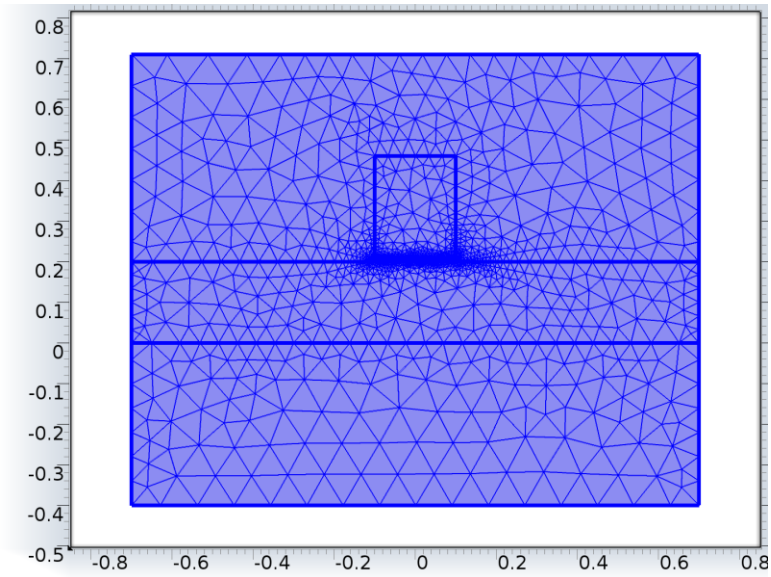


Initial Values 1

Selection

Geometric entity level	Domain
Selection	Domains 1–5

2.5 Mesh 1



Mesh 1

2.5.1 Size (size)

Settings

Name	Value
Maximum element size	.1
Minimum element size	.01
Resolution of curvature	0.25
Resolution of narrow regions	6
Maximum element growth rate	2
Predefined size	Finer
Custom element size	Custom

3 Study 1

3.1 Mode Analysis

Mesh selection

Geometry	Mesh
Geometry 1 (geom1)	mesh1

Physics selection

Physics	Discretization
Electromagnetic Waves (emw)	physics

3.2 Solver Configurations

3.2.1 Solver 1

Compile Equations: Mode Analysis (st1)

Study and step

Name	Value
Use study	Study 1
Use study step	Mode Analysis

Dependent Variables 1 (v1)

General

Name	Value
Defined by study step	Mode Analysis

Initial values of variables solved for

Name	Value
Solution	Zero

Values of variables not solved for

Name	Value
Solution	Zero

mod1.E (mod1_E)

General

Name	Value

Name	Value
Field components	{mod1.Ex, mod1.Ey, mod1.Ez}

Eigenvalue Solver 1 (e1)

General

Name	Value
Defined by study step	Mode Analysis
Desired number of eigenvalues	1
Eigenvalue transformation	Effective mode index
Value	nSeed

Values of linearization point

Name	Value
Solution	Zero

Advanced (aDef)

General

Name	Value
Allow complex-valued output from functions with real input	On

4 Results

4.1 Data Sets

4.1.1 Solution 1

Selection

Geometric entity level	Domain
Selection	Geometry geom1

Solution

Name	Value
Solution	Solver 1
Model	Save Point Geometry 1

4.1.2 Cut Line 2D 1

Data

Name	Value
Data set	Solution 1

Advanced

Name	Value
Space variable	cln1x

4.1.3 Cut Line 2D 2

Data

Name	Value
Data set	Solution 1

Advanced

Name	Value
Space variable	cln2x

4.2 Tables

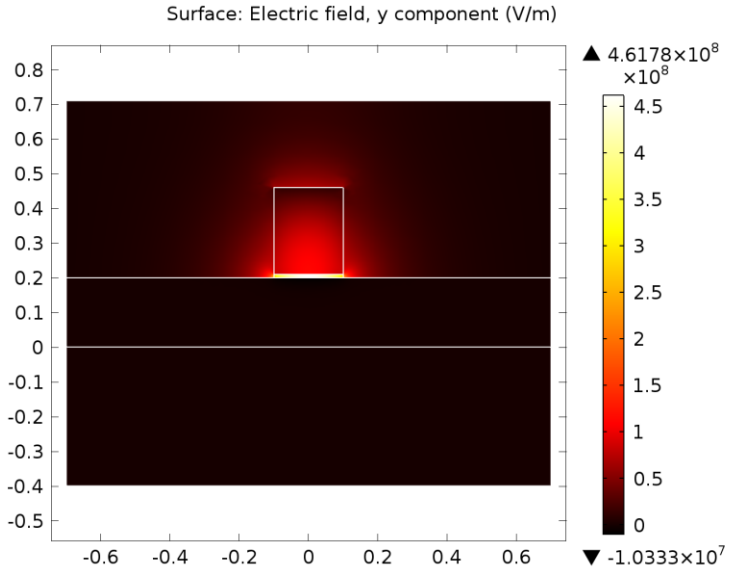
4.2.1 Evaluation 2D

Interactive 2D values
Evaluation 2D

x	y	Value
-0.38667	-0.11904	2871.62094
-0.47178	0.54873	5.72569e9

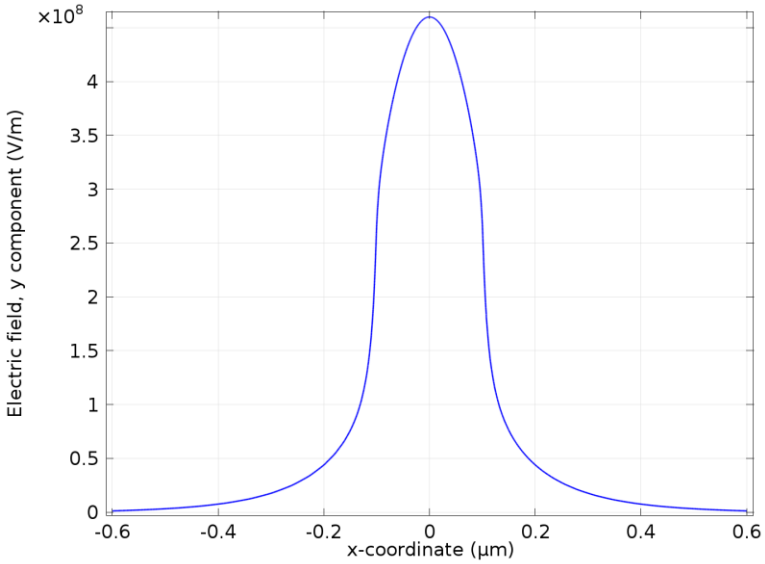
4.3 Plot Groups

4.3.1 Electric Field (emw)

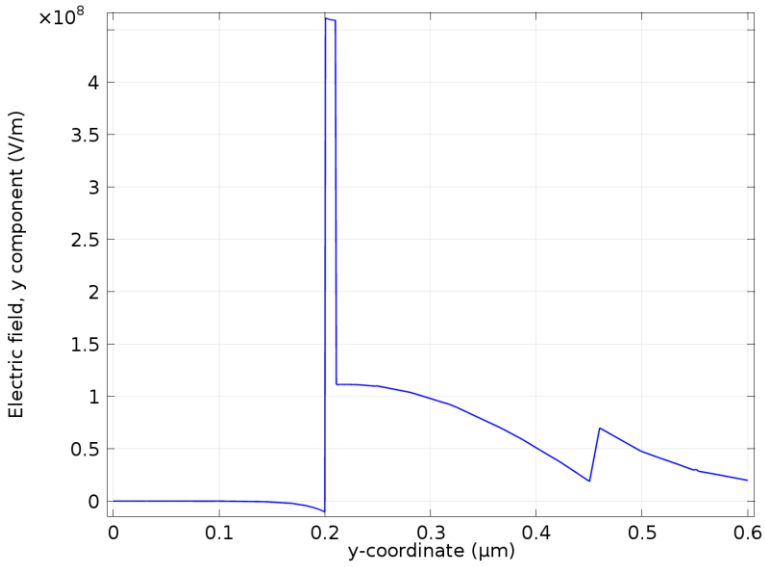


Surface: Electric field, y component (V/m)

4.3.2 1D Plot Group 2



4.3.3 1D Plot Group 3



Appendix B: Frequency Domain Simulation Report

This appendix presents a full report, which generated by using COMSOL software, about the frequency domain simulation procedure used in this work to study the transmission characteristics of the nonlinear ring resonator device. This report involves four steps, which are the same as the mode-solving simulation report mentioned in Appendix A, except that the physical studies used here are boundary mode analysis and frequency domain analysis. The first physical study is the boundary mode analysis, which tells COMSOL to find the appropriate numerical modes at the two ports in the boundaries of the input waveguide. This physical study is link to the frequency domain study in order to study the transmission of the propagating modes.

Contents

1. Global Definitions....71
   1.1. Parameters 1....71
2. Model 1 (mod1)....72
   2.1. Definitions....72
   2.2. Geometry 1....72
   2.3. Materials....74
   2.4. Electromagnetic Waves, Frequency Domain (emw)....76
   2.5. Mesh 1....81
3. Study 1....82
   3.1. Boundary Mode Analysis....82
   3.2. Boundary Mode Analysis 2....82
   3.3. Frequency Domain....82
   3.4. Solver Configurations....82
4. Results....90
   4.1. Data Sets....90
   4.2. Plot Groups....91

1 Global Definitions

1.1 Parameters 1

Parameters

Name	Expression	Description
WD	10	Domain width
h1	2	cladding 1
h2	5	cladding 2
NcR	3.095	core index, real
NcI	.003417	core index, imaginary
NclR	1.4579	cladding index, real
NclI	.000307	cladding index, imaginary
Wc	.2	waveguide thickness
wl	1.55	free space wavelength
neffx	2.416678	effective index of the mode
d	.25	separation distance
Rin	(r) - (hc/2)	inner radius of the RR
Rou	(r) + (hc/2)	outer radius of the resonator
r	1	Ring radius
f0	3e14/wl	frequency

2 Model 1 (mod1)

2.1 Definitions

2.1.1 Coordinate Systems

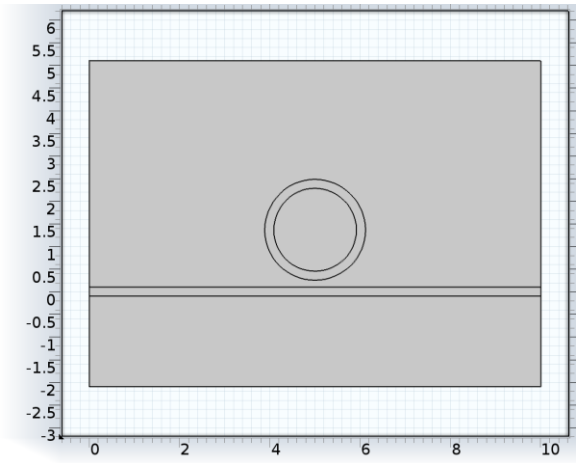
Boundary System 1

Coordinate system type	Boundary system
Identifier	sys1

Settings

Name	Value
Coordinate names	{t1, n, to}
Create first tangent direction from	Global Cartesian

2.2 Geometry 1



Geometry 1

units

Length unit	µm
Angular unit	deg

Geometry statistics

Property	Value
Space dimension	2
Number of domains	5
Number of boundaries	18

2.2.1 cladd (r1)

Position

Name	Value
Position	{0, h1 - (hc/2)}
Width	WD
Height	h1
Size	{WD, h1}

2.2.2 core (r2)

Position

Name	Value
Position	{0, hc/2}
Width	WD
Height	hc
Size	{WD, hc}

2.2.3 upper cladd (r3)

Position

Name	Value
Position	{0, hc/2}
Width	WD
Height	h2
Size	{WD, h2}

2.2.4 outer circle (c1)

Position

Name	Value
Position	{WD/2, d + hc + Rin}
Radius	Rou

2.2.5 Circle 2 (c2)

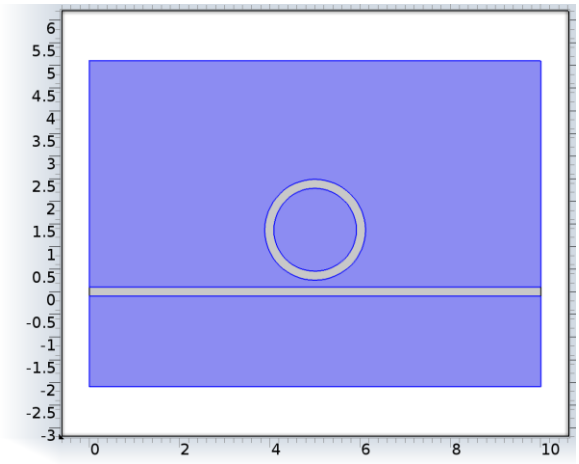
Position

Name	Value
Position	{WD/2, Rin + hc + d}

Name	Value
Radius	Rin

2.3 Materials

2.3.1 cladding



cladding

Selection

Geometric entity level	Domain
Selection	Domains 1, 3, 5

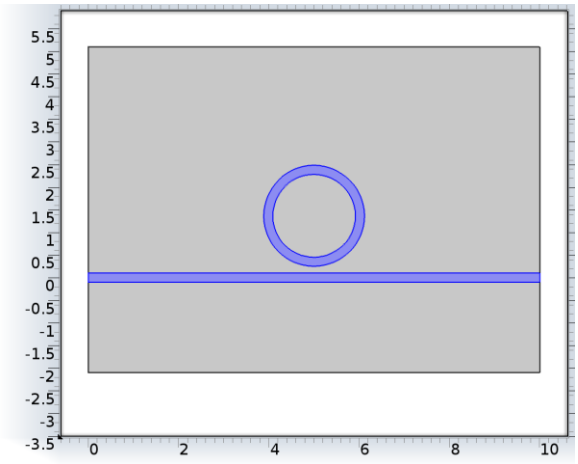
Material parameters

Name	Value	Unit
Refractive index	NclR	1
Refractive index, imaginary part	NclI	1

Refractive index Settings

Description	Value
Refractive index	{{NclR, 0, 0}, {0, NclR, 0}, {0, 0, NclR}}
Refractive index, imaginary part	{{NclI, 0, 0}, {0, NclI, 0}, {0, 0, NclI}}

2.3.2 core



core

Selection

Geometric entity level	Domain
Selection	Domains 2, 4

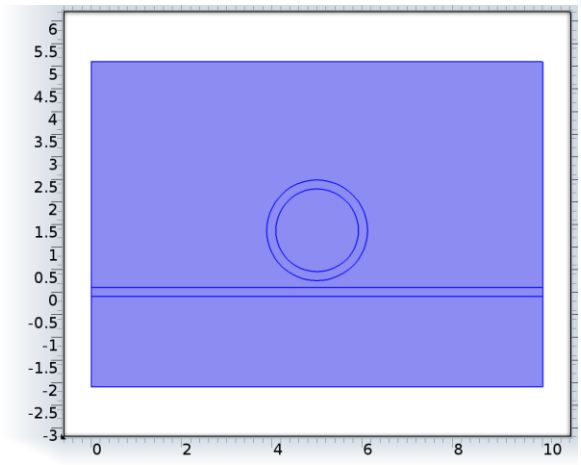
Material parameters

Name	Value	Unit
Refractive index	NcR	1
Refractive index, imaginary part	NcI	1

Refractive index Settings

Description	Value
Refractive index	{{NcR, 0, 0}, {0, NcR, 0}, {0, 0, NcR}}
Refractive index, imaginary part	{{NcI, 0, 0}, {0, NcI, 0}, {0, 0, NcI}}

2.4 Electromagnetic Waves, Frequency Domain (emw)



Electromagnetic Waves, Frequency Domain

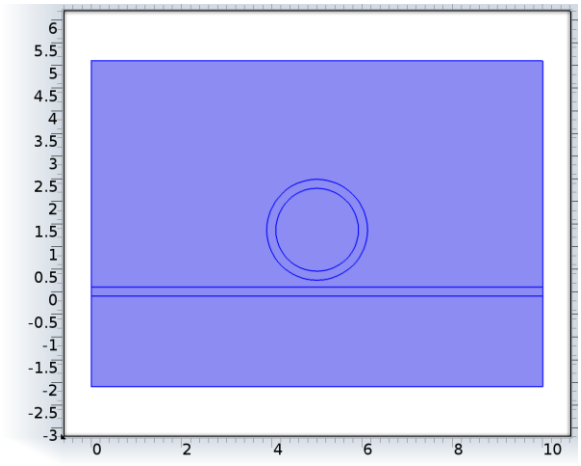
Selection

Geometric entity level	Domain
Selection	Domains 1–5

Equations

$$\nabla \times \mu_r^{-1}(\nabla \times \mathbf{E}) - k_0^2(\epsilon_r - \frac{j\sigma}{\omega\epsilon_0})\mathbf{E} = \mathbf{0}$$

2.4.1 Wave Equation, Electric 1



Wave Equation, Electric 1

Selection

Geometric entity level	Domain
Selection	Domains 1–5

Equations

$$\nabla \times (\nabla \times \mathbf{E}) - k_0^2 \varepsilon_r \mathbf{E} = 0$$

Settings

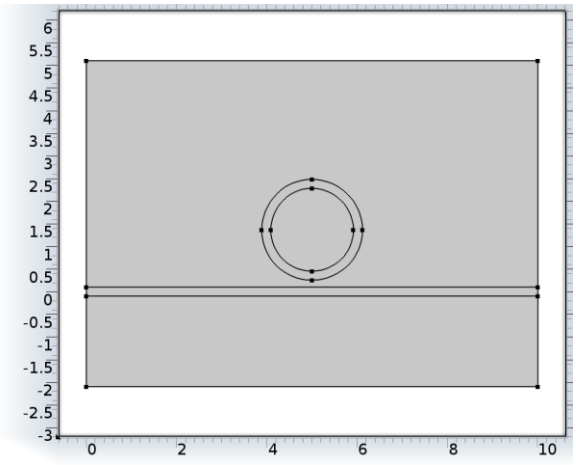
Settings

Description	Value
Electric displacement field model	Refractive index

Properties from material

Property	Material	Property group
Refractive index	cladding	Refractive index
Refractive index, imaginary part	cladding	Refractive index
Refractive index	core	Refractive index
Refractive index, imaginary part	core	Refractive index

2.4.2 Perfect Electric Conductor 1



Perfect Electric Conductor 1

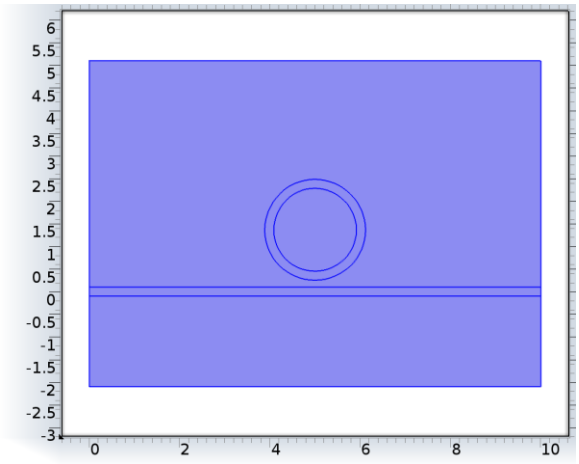
Selection

Geometric entity level	Boundary
Selection	No boundaries

Equations

$$\mathbf{n} \times \mathbf{E} = 0$$

2.4.3 Initial Values 1

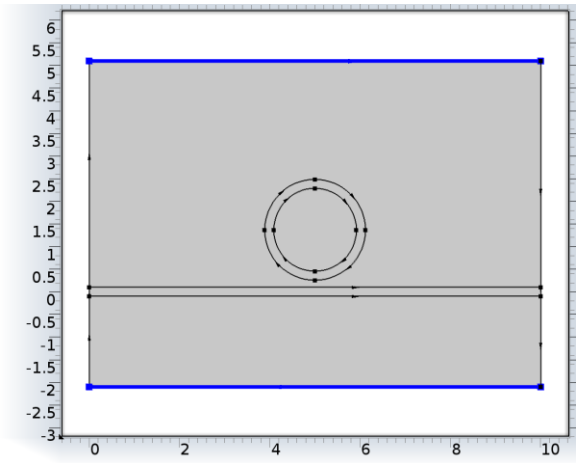


Initial Values 1

Selection

Geometric entity level	Domain
Selection	Domains 1–5

2.4.4 Scattering Boundary Condition 1



Scattering Boundary Condition 1

Selection

Geometric entity level	Boundary
Selection	Boundaries 2, 7

Equations

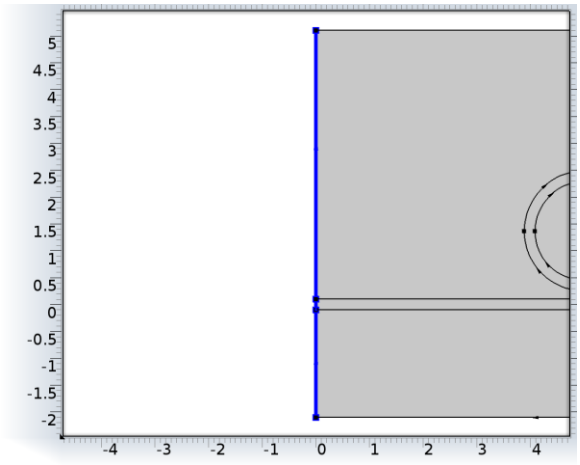
$$\mathbf{n} \times (\nabla \times \mathbf{E}) - jk\mathbf{n} \times (\mathbf{E} \times \mathbf{n}) = -\mathbf{n} \times (\mathbf{E}_0 \times (jk(\mathbf{n} - \mathbf{k}_{dir}))) e^{-j\mathbf{k}_{dir} \cdot \mathbf{r}}$$

Settings

Settings

Description	Value
Wave direction	{((nx)), ((ny)), 0}

2.4.5 Port 1



Port 1

Selection

Geometric entity level	Boundary
Selection	Boundaries 1, 3, 5

Equations

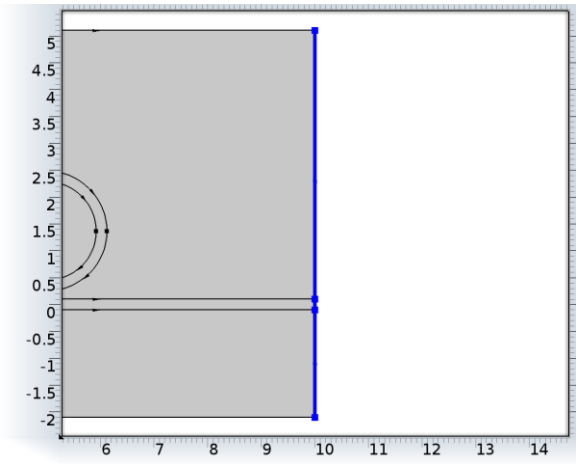
$$\mathbf{n} \times \nabla \times \mathbf{E} - j\beta \mathbf{n} \times \mathbf{E} \times \mathbf{n} = \mathbf{0}$$

Settings

Settings

Description	Value
Wave excitation at this port	On
Port input power	0.001
Type of port	Numeric

2.4.6 Port 2



Port 2

Selection

Geometric entity level	Boundary
Selection	Boundaries 8–10

Equations

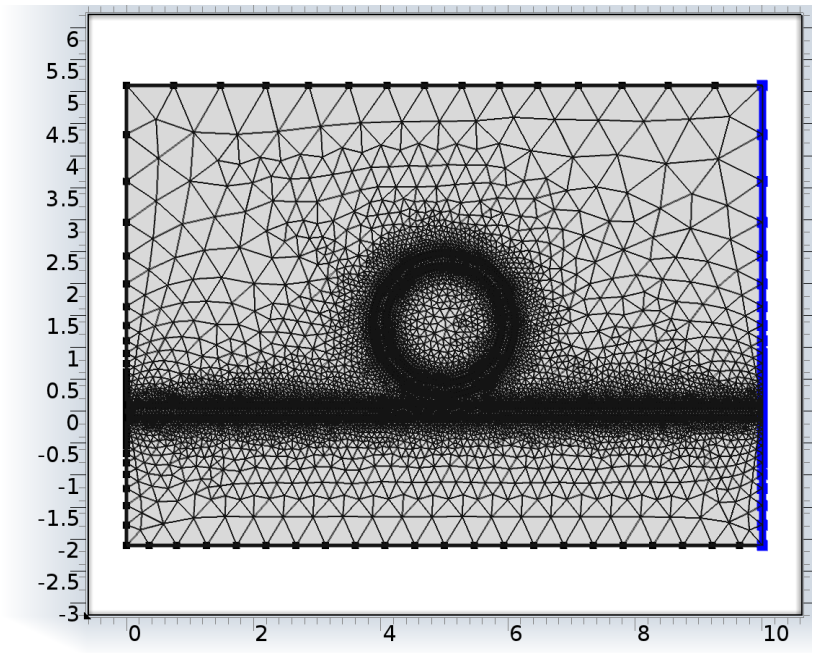
$$\mathbf{n} \times \nabla \times \mathbf{E} - j\beta \mathbf{n} \times \mathbf{E} \times \mathbf{n} = \mathbf{0}$$

Settings

Settings

Description	Value
Port name	2
Type of port	Numeric

2.5 Mesh 1



Mesh 1

2.5.1 Size (size)

Settings

Name	Value
Maximum element size	0.8
Minimum element size	.003
Resolution of curvature	0.25
Resolution of narrow regions	6
Maximum element growth rate	1.2
Predefined size	Extra fine
Custom element size	Custom

3 Study 1

3.1 Boundary Mode Analysis

Mesh selection

Geometry	Mesh
Geometry 1 (geom1)	mesh1

Physics selection

Physics	Discretization
Electromagnetic Waves, Frequency Domain (emw)	physics

3.2 Boundary Mode Analysis 2

Mesh selection

Geometry	Mesh
Geometry 1 (geom1)	mesh1

Physics selection

Physics	Discretization
Electromagnetic Waves, Frequency Domain (emw)	physics

3.3 Frequency Domain

Frequencies: 3e14/wl

Mesh selection

Geometry	Mesh
Geometry 1 (geom1)	mesh1

Physics selection

Physics	Discretization
Electromagnetic Waves, Frequency Domain (emw)	physics

3.4 Solver Configurations

3.4.1 Solver 1

Compile Equations: Boundary Mode Analysis (st1)

Study and step

Name	Value

Name	Value
Use study	Study 1
Use study step	Boundary Mode Analysis

Dependent Variables 1 (v1)

General

Name	Value
Defined by study step	User defined

Initial values of variables solved for

Name	Value
Solution	Zero

Values of variables not solved for

Name	Value
Solution	Zero

mod1.emw.Ebm1 (mod1_emw_Ebm1)

General

Name	Value
Field components	{mod1.emw.Ebm1x, mod1.emw.Ebm1y, mod1.emw.tEbm1z}

mod1.emw.Ebm2 (mod1_emw_Ebm2)

General

Name	Value
Field components	{mod1.emw.Ebm2x, mod1.emw.Ebm2y, mod1.emw.tEbm2z}
Solve for this field	off

mod1.emw.nebm1 (mod1_emw_nebm1)

General

Name	Value
Field components	mod1.emw.nebm1

mod1.emw.nebm2 (mod1_emw_nebm2)

General

Name	Value

Name	Value
Field components	mod1.emw.nebm2
Solve for this field	off

mod1.E (mod1_E)

General

Name	Value
Field components	{mod1.Ex, mod1.Ey, mod1.Ez}
Solve for this field	off

mod1.Sparam1 (mod1_Sparam1)

General

Name	Value
State components	mod1.emw.S1x
Solve for this state	off
State name	mod1_Sparam1

mod1.Sparam2 (mod1_Sparam2)

General

Name	Value
State components	mod1.emw.S2x
Solve for this state	off

Eigenvalue Solver 1 (e1)

General

Name	Value
Defined by study step	Boundary Mode Analysis
Desired number of eigenvalues	1
Eigenvalue transformation	Effective mode index
Value	NcR

Values of linearization point

Name	Value
Solution	Zero

Advanced (aDef)

General

Name	Value
Allow complex-valued output from functions with real input	On

Store Solution 2 (su1)

General

Name	Value
Solution	Store Solution 2

Compile Equations: Boundary Mode Analysis 2 (2) (st2)

Study and step

Name	Value
Use study	Study 1
Use study step	Boundary Mode Analysis 2

Dependent Variables 2 (v2)

General

Name	Value
Defined by study step	User defined

Initial values of variables solved for

Name	Value
Method	Solution
Solution	Solver 1

Values of variables not solved for

Name	Value
Method	Solution
Solution	Solver 1

mod1.emw.Ebm1 (mod1_emw_Ebm1)

General

Name	Value
Field components	{mod1.emw.Ebm1x, mod1.emw.Ebm1y, mod1.emw.tEbm1z}
Solve for this field	off

mod1.emw.Ebm2 (mod1_emw_Ebm2)

General

Name	Value
Field components	{mod1.emw.Ebm2x, mod1.emw.Ebm2y, mod1.emw.tEbm2z}

mod1.emw.nebm1 (mod1_emw_nebm1)

General

Name	Value
Field components	mod1.emw.nebm1
Solve for this field	off

mod1.emw.nebm2 (mod1_emw_nebm2)

General

Name	Value
Field components	mod1.emw.nebm2

mod1.E (mod1_E)

General

Name	Value
Field components	{mod1.Ex, mod1.Ey, mod1.Ez}
Solve for this field	off

mod1.Sparam1 (mod1_Sparam1)

General

Name	Value
State components	mod1.emw.S1x
Solve for this state	off
State name	mod1_Sparam1

mod1.Sparam2 (mod1_Sparam2)

General

Name	Value
State components	mod1.emw.S2x
Solve for this state	off

Eigenvalue Solver 2 (e2)

General

Name	Value
Defined by study step	Boundary Mode Analysis 2
Desired number of eigenvalues	1
Eigenvalue transformation	Effective mode index
Value	NcR

Values of linearization point

Name	Value
Solution	Zero

Advanced (aDef)

General

Name	Value
Allow complex-valued output from functions with real input	On

Store Solution 3 (su2)

General

Name	Value
Solution	Store Solution 3

Compile Equations: Frequency Domain (3) (st3)

Study and step

Name	Value
Use study	Study 1
Use study step	Frequency Domain

Dependent Variables 3 (v3)

General

Name	Value
Defined by study step	Frequency Domain

Initial values of variables solved for

Name	Value
Method	Solution

Name	Value
Solution	Solver 1

Values of variables not solved for

Name	Value
Method	Solution
Solution	Solver 1

mod1.emw.Ebm1 (mod1_emw_Ebm1)

General

Name	Value
Field components	{mod1.emw.Ebm1x, mod1.emw.Ebm1y, mod1.emw.tEbm1z}
Solve for this field	off

mod1.emw.Ebm2 (mod1_emw_Ebm2)

General

Name	Value
Field components	{mod1.emw.Ebm2x, mod1.emw.Ebm2y, mod1.emw.tEbm2z}
Solve for this field	off

mod1.emw.nebm1 (mod1_emw_nebm1)

General

Name	Value
Field components	mod1.emw.nebm1
Solve for this field	off

mod1.emw.nebm2 (mod1_emw_nebm2)

General

Name	Value
Field components	mod1.emw.nebm2
Solve for this field	off

mod1.E (mod1_E)

General

Name	Value

Name	Value
Field components	{mod1.Ex, mod1.Ey, mod1.Ez}

mod1.Sparam1 (mod1_Sparam1)

General

Name	Value
State components	mod1.emw.S1x
State name	mod1_Sparam1

mod1.Sparam2 (mod1_Sparam2)

General

Name	Value
State components	mod1.emw.S2x

Stationary Solver 1 (s1)

General

Name	Value
Defined by study step	Frequency Domain

Advanced (aDef)

General

Name	Value
Allow complex-valued output from functions with real input	On

Parametric 1 (p1)

General

Name	Value
Defined by study step	Frequency Domain
Parameter value list	3e14/wl

Fully Coupled 1 (fc1)

General

Name	Value
Linear solver	Direct

4 Results

4.1 Data Sets

4.1.1 Solution 1

Selection

Geometric entity level	Domain
Selection	Geometry geom1

Solution

Name	Value
Solution	Solver 1
Model	Save Point Geometry 1

4.1.2 Solution 2

Selection

Geometric entity level	Domain
Selection	Geometry geom1

Solution

Name	Value
Solution	Store Solution 2
Model	Save Point Geometry 1

4.1.3 Solution 3

Selection

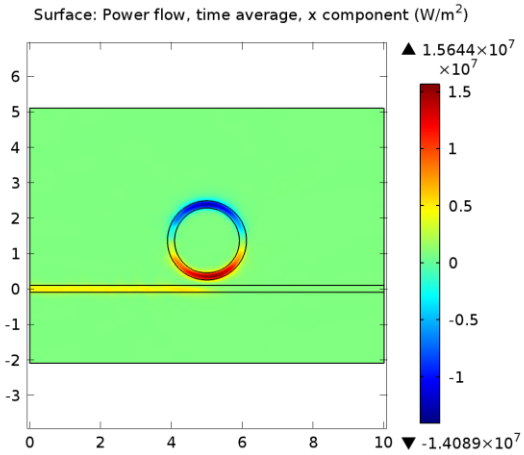
Geometric entity level	Domain
Selection	Geometry geom1

Solution

Name	Value
Solution	Store Solution 3
Model	Save Point Geometry 1

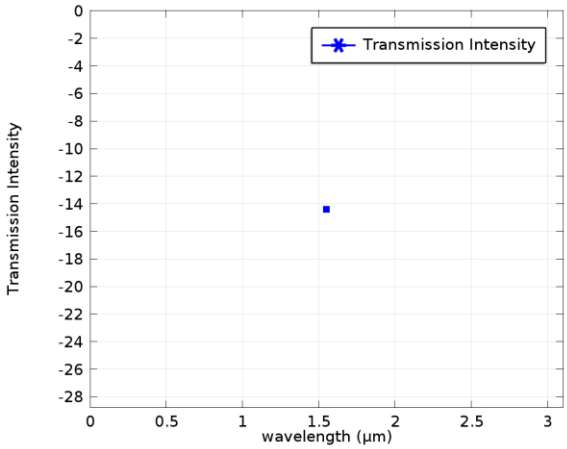
4.2 Plot Groups

4.2.1 Electric field



Surface: Power flow, time average, x component (W/m^2)

4.2.2 1D Plot Group 2



Appendix C: Matlab Code of 2D Scan

This appendix presents a Matlab code used in this work; it is a 2D scan code. The purpose from this code is to study the effect of the waveguide parameters H_s and W on the parameters that measure the performance of the nonlinear hybrid plasmonic waveguide such as L_p, A_{eff}, $\bar{n}_2$, γ, and F.

```
% 2D_SCAN_Code.m

clearvars -except model;

% avoids re-loading mph file (COMSOL file) if it already exists
% Clear manually if the file has changed in any way.

close all; format compact;

%FILE VARIABLES (path and name of the relevant COMSOL mph file)

file.Path='C:\Users\Mohammed\Desktop\matlabi\';

% THIS IS MU PATH,,CHANGE IT TO YOUR PATH!!

file.Name='2D_scan';

% VARIABLES RELATED TO THE PARAMETER SCAN

scanvars.ScanVect=linspace(.1,.35,21);

%define the waveguide height as a vector
scanvars.COMParam='H';

% parameter name (to pass to COMSOL)
scanvars.PlotLabel='H_S';

% label (for plotting purposes only)
scanvars.PlotTitle='Silicon Ridge Height';

% label (or display purposes only on command window)
scanvars.ScanVect1=linspace(.1,.3,21);
% define the waveguide width as a vector
scanvars.COMParam1='W';

% parameter name (to pass to COMSOL)
scanvars.PlotLabel1='W';

% label (for plotting purpose only)
scanvars.PlotTitle1='Ridge Width';
```

```
[scanvars.XPLOT,scanvars.YPLOT]=meshgrid(scanvars.ScanVect, ...
    scanvars.ScanVect1);
% For 2D plot purposes

% ADDITIONAL MODELING VARIABLES

modvars.CoreDomain=4;
% Domain index for core material in COMSOL file. This is required for the
% post-processing (to tell MATLAB where the nonlinearity exists)

modvars.nSeed=2.69;
% initial seed index (so we only need to search for one mode in COMSOL)

% WAVEGUIDE PARAMETERS USED ONLY IN POSTPROCESSING (not passed to COMSOL)
Z0=377;             % Free-space impedance (Ohms)
n2=2.2e-16;         % core nonlinear index coefficient (m^2/W)
nnl=1.7;           % linear index of nonlinear medium


% LOAD COMSOL MODEL,
if exist('model')==0
    disp(['Loading COMSOL file ',file.FullName]);
    model = mphload(file.FullName);
end

% DISPLAY THE FIELD MAGNITUDE IN THE WAVEGUIDE (just to check that you are
looking at the right structure).
 figure(1)
 mphplot(model,'pg1', 'rangenum' ,1);
 title('|E|'); axis tight; pause(1);
 set(gca,'XTick',[],'YTick',[],'XTickLabel',[],'YTickLabel',[]);

% TIME MANAGEMENT INITIALIZATION
startTime=cputime;
counter=0;
totalSims=length(scanvars.ScanVect)*length(scanvars.ScanVect1);

% LOOP THROUGH THE PARAMETER BEING SCANNED
for N=1:length(scanvars.ScanVect),
    for M=1:length(scanvars.ScanVect1),
    counter=counter+1;      % for display purposes only
    % UPDATE THE DISPLAY
    disp('----------------------------');
    disp(['Simulating Waveguide ',num2str(counter),' of ' , ...
        num2str(totalSims),': ',scanvars.PlotTitle,' = ' ...
        ,num2str(scanvars.ScanVect(N)),', ',scanvars.PlotTitle1, ...
        ' = ',num2str(scanvars.ScanVect1(M))]);
    disp(['Seed Index: ',num2str(modvars.nSeed)]);

    % TELL COMSOL THE SEED INDEX AND THE NEW PARAMETER VALUE
    model.param.set('nSeed',modvars.nSeed);
    model.param.set(scanvars.COMParam,scanvars.ScanVect(N));
    model.param.set(scanvars.COMParam1,scanvars.ScanVect1(M));
```

```
    % RUN THE COMSOL SIMULATION
    model.sol('sol1').run;

    % EXTRACT AND DISPLAY RESULTS FROM THE COMSOL SIMLUATION
    wl=2*pi/mphglobal(model,'emw.k0');
    % by extracting k0 from COMSOL for example, so the wavelength can be
determined

        disp(['wavelength = ',num2str(wl*1e9),' nm'])
    k0=2*pi/wl;

    % calculating the wavenumber
    neffI(N,M)=abs(1*mphglobal(model,'emw.dampz')/k0);

    % by extracting dampz from COMSOL, for example, we can determine
    %the imaginary part of neff
        disp(['neff(Imag) = ',num2str(neffI(N,M))])
    alpha(N,M)=2*k0*neffI(N,M);

    % the loss coefficient

    PropLength(N,M)=1/(2*k0*neffI(N,M));
        disp(['Propagation Length = ',num2str(PropLength(N,M)*1e6), ...
            ' microns'])

    % Calculating propagation length Lp

    neffR(N,M)=mphglobal(model,'emw.neff');
        disp(['neff(Real) = ',num2str(neffR(N,M))])

    % extracting the real part of the mode effective index neff

    % Next,Calculating the NONLINEAR FIGURES OF MERIT:

    % first calculating the effective mode area Aeff

    nlDen=mphint(model,'(Ex*conj(emw.Hy)- ...
    Ey*conj(emw.Hx))*abs(Ex*conj(emw.Hy)-Ey*conj(emw.Hx))');

    % the denominator of the Aeff

    nlNum1=mphint(model,'Ex*conj(emw.Hy)-Ey*conj(emw.Hx)');
    nlNum=nlNum1.*conj(nlNum1);

    % the numerator of Aeff

    Aeff(N,M)=real(nlNum/nlDen);

    % the value of Aeff
        disp(['NL Effective Area = ',num2str(Aeff(N,M)*1e12), ...
            ' square microns'])
        % for display purpose on command window
    % Second, calculating the effective nonlinear index coefficient n2bar
```

```
    n2numInt=mphint(model, ...

'2*(Ex*conj(Ex)+Ey*conj(Ey)+Ez*conj(Ez))^2+(abs(Ex^2+Ey^2+Ez^2))^2'
    ,'Selection',modvars.CoreDomain);

    % the numerator of n2bar

    n2bar(N,M)=real(n2*nnl^2/Z0^2*n2numInt/(3*nlDen));
        disp(['n2Bar = ',num2str(n2bar(N,M)),' m^2/W, n2bar/n2 = ',num2str
            (n2bar(N,M)/n2)])

        % n2bar value

    % Third,calculating the kerr nonlinear coefficient, gamma
    gamma(N,M)=k0*n2bar(N,M)/Aeff(N,M);
        disp(['gamma = ',num2str(gamma(N,M)),' (W.m)^-1']);
        disp(['gamma*L = ',num2str(gamma(N,M).*PropLength(N,M)),
            ' (W.m)^-1.um'])


    % TIME MANAGEMENT...ESTIMATES THE REMAINING TIME FOR THE SCAN,

    elapsed=cputime-startTime;
    disp(['Simulation time = ',num2str(elapsed),' seconds'])
    startTime=cputime;

remainingTimes=(length(scanvars.ScanVect)*length(scanvars.ScanVect1))..
    -((N-1)*length(scanvars.ScanVect1)+M);
    remainingSeconds=elapsed*remainingTimes;
    remainingMinutes=floor(remainingSeconds/60);
    remainingSeconds2=mod(remainingSeconds,60);
    disp(['Estimated time remaining = ',num2str(remainingMinutes), ...
        ' minutes, ',num2str(round(remainingSeconds2)),' seconds'])
    if M==1
        % if this simulation was the first point in a row, remember
neffR..
        %for later use
       savednSeed=neffR(N,M);
    end

    if M==length(scanvars.ScanVect1)
        % if this simulation was the last point in a row, set nSeed to ...
        %the one from the beginning of the row
       modvars.nSeed=savednSeed;
    else
        % otherwise, use the nSeed from the previous simulation
       modvars.nSeed=neffR(N,M);
    end
    end  % end of inner loop (M)

end  % end of outer loop (N)

% Finally, visualizing the results as 2D plot,,
% PLOT VARIOUS WAVEGUIDE PARAMETERS AS A
```

```
% FUNCTION OF THE SCAN VARIABLE, AFTER THE SCAN IS COMPLETE
figure(2)
subplot(3,2,1)
pcolor(scanvars.XPLOT,scanvars.YPLOT,neffR);  xlabel(scanvars.PlotLabel,
..
'fontsize',13); ylabel(scanvars.PlotLabel1,'fontsize',13); ...
    title('n_{eff}','fontsize',12);axis tight;shading interp;
colorbar

% PLOTTING THE EFFECIVE MODE INDEX VERSUS Hs AND W (waveguides
parameteres)

subplot(3,2,2)
pcolor(scanvars.XPLOT,scanvars.YPLOT,Aeff.*1e12);
xlabel(scanvars.PlotLabel
,'fontsize',13); ylabel(scanvars.PlotLabel1,'fontsize',13);
title('A_{eff} [\mum^2]','fontsize',12);axis tight;shading interp;
colorbar

% PLOTTING THE EFFECTIVE MODE AREA VERSUS Hs AND W

subplot(3,2,3)
pcolor(scanvars.XPLOT,scanvars.YPLOT,gamma); xlabel(scanvars.PlotLabel,...
'fontsize',13); ylabel(scanvars.PlotLabel1,'fontsize',13);
title('\gamma [W^{-1}m^{-1}]','fontsize',12);axis tight;shading interp;
colorbar

% PLOTTING THE KERR NONLINEAR COEFFIECIIENT (GAMMA) VERSUS Hs AND W

subplot(3,2,4)
pcolor(scanvars.XPLOT,scanvars.YPLOT,PropLength.*1e6);
xlabel(scanvars.PlotLabel,'fontsize',13); ylabel(scanvars.PlotLabel1, ...
'fontsize',13);title('Propagation Length [\mum]','fontsize',12);
axis tight;shading interp;
colorbar

% PLOTTING THE PROPAGATION LENGTH VERSUS Hs AND W

subplot(3,2,5)
pcolor(scanvars.XPLOT,scanvars.YPLOT,n2bar./n2);
xlabel(scanvars.PlotLabel,'fontsize',13); ylabel(scanvars.PlotLabel1, ...
'fontsize',13);title('$\overline{n}_2/n_2$','interpreter','latex', ...
'fontsize',12); axis tight;shading interp;
colorbar

% PLOTTING THE EFFECTIVE NONLINEAR INDEX COEFFIECNT n2bar VERSUS Hs AND W

subplot(3,2,6)
pcolor(scanvars.XPLOT,scanvars.YPLOT,gamma.*PropLength.*1e6);
xlabel(scanvars.PlotLabel,'fontsize',13); ylabel(scanvars.PlotLabel1, ...
'fontsize',13);title('F [W^{-1}m^{-1}\mum]','fontsize',12);
axis tight;shading interp;
colorbar
```

```
% PLOTTING THE NONLEAR FIGURE OF MERIT (F) VERSUS Hs AND W
% SAVE WORKSPACE VARIABLES

save 2D_SCAN_Code.mat
```

Bibliography

[1] W. F. Brinkman, D. E. Haggan, and W. W. Troutman, “A History of the Invention of the transistor and where it will lead us,” IEEE J Solid-St Circ, vol. 32, no. 12, pp. 1858-1864 (1997).

[2] J.A. Conway, S. Sahni, and T. Szkopek, “Plasmonic interconnects versus conventional interconnects a comparison of latency, cross-talk and energy costs,” Opt. Express, vol. 15, no. 8, pp. 4474-4484 (2007).

[3] W. L. Ha, R. M. Fortenberry, and R. S. Tucker, “Demonstration of photonic fast packet switching at 700 Mbit/s data rate," Electron. Lett., vol. 27, no. 10, pp. 789-790 (1991).

[4] E. Ozbay, “Plasmonics: Merging Photonics and Electronics at Nanoscale Dimensions,” Science, vol.311, pp. 189-193 (2006).

[5] E. Suhir, “Microelectronics and photonics: the future,” Microelectr J, vol.31, pp. 839-951 (2000).

[6] E. A. J. Marcatili, “Bends in optical dielectric guides,” Bell Syst. Tech. J., vol.48, no. 7, pp. 2103-2132 (1969).

[7] Y. A. Vlasov and S. J. Mcnab, “Losses in single-mode silicon-on-insulator strip waveguides and bends,” Opt. Express, vol. 12, no. 8, pp. 1622-1631 (2004).

[8] A. streltsov, N. Borrelli, J. Dickinson, T. Kiczenski, S. Logunov, and J. Schroeder, “Laser-written high-contrast waveguides in glass,” Proc. of Spie, vol. 7366,no. 11, pp. 1-8 (2010).

[9] J. Takahar, S. Yamagishi, H. Taki, A. Morimoto, and T. Kobayashi, “Guiding of a one-dimensional optical beam with nanometer diameter,” Opt. Express, vol. 22, no. 7, pp. 475-477 (1997).

[10] M. L. Brongersma and V. M. Shalaev, “The Case for Plasmonics,” Science, vol. 328, no. 5977, pp. 440-441(2010).

[11] S. A. Maier and H. A. Atwater, “Plasmonic: localization and guiding of electromagnetic energy in metal/dielectric structures,” J. Appl. Phys., vol. 98, 011101 (2005).

[12] W. L. Barnes, A. Dereux, and T. W. Ebbesen, “Surface Plasmon subwavelength optics,” Nature, vol. 424, pp. 824-830 (2003).

[13] R. H. Ritchie, “Plasma losses by fast electrons in thin films," Phys. Rev., vol. 106, no. 5, pp. 874-881 (1957).

[14] C. J. Powell, J. B. Swan, “Origin of the characteristic electron energy losses in aluminum,” Phys. Rev., vol. 115, no. 4, pp. 869-875 (1959).

[15] E. Kretschmann, H. Raether, “Radiative decay of nonradiative surface plasmons excited by light,” *Z.* Naturforsch*.,* vol. A 23, no. 12, pp. 2135–2136 (1968).

[16] Otto, “Excitation of nonradiative plasma surface waves in silver by method of frustrated total reflection,” Z. Phys., vol. 216, pp. 398-410 (1968).

[17] J. R. Sambles, G. W. Bradbery, and Fuzi Yang, “Optical-excitation of surface-plasmons an introduction,” Contemp. Phys., vol. 32, pp. 173-183 (1991).

[18] R. H. Ritchie, E. T. Arakawa, J. J. Cowan, and R. N. Hamm, “Surface Plasmon resonance effect in grating diffraction,” Phys. Rev. Lett., vol. 21, no. 22, pp. 1530-1533 (1968).

[19] P. T. Worthing and W. L. Barnes, “Efficient coupling of surface plasmon polaritons to radiation using a bigrating,” Appl. Phys. Lett., vol. 79, no. 19, pp. 3035-3037 (2001).

[20] S. A. Maier, “Plasmonics: Fundamentals And Applications”, ISBN 978-0387-33150-8, Springer (2007), Chapter-2, pp.(25-27).

[21] A.V. Zayats et al*.,* “Nano-optics of surface plasmon polaritons,” vol. 408, pp.131-314 (2005).

[22] L. Novotny and B. Hecht, *Principles of Nano-Optics* (University Press, Cambridge, 2006), pp.386-387.

[23] B. Hecht, H. Bielefeltdt, L. Novotny, Y. Inouye, and D. W. Pohl, “Local excitation, scattering, and interference of surface plasmons,” Phys. Rev. Lett., vol. 77, no. 9, pp. 1889-1892 (1996).

[24] Brecht and G. Gauglitz, “Optical probes and transducers,” Biosens. Bioelectron, vol. 10, pp. 923–936 (1995).

[25] J. Homola, “Optical fiber sensor based on surface Plasmon excitation,” Sensor. Actuator, vol. B 29, pp. 401-405 (1995).

[26] D. F. P. Pile and D. K. Gramotnev, “Channel plasmon–polariton in a triangular groove on a metal surface,” Opt. Lett., vol. 29, no. 10, pp. 1069-1071 (2004).

[27] E. Moreno, F. J. Garcia-Vidal, S. G. Rodrigo, L. Martin-Moreno, and S.I. Bozhevolnyi, “Channel plasmon-polaritons: modal shape, dispersion, and losses,” Opt. Lett., vol. 31, no. 23, pp. 3447-3449 (2006).

[28] S. I. Bozhevolnyi, V. S. Volkov, E. Devaux, J. Y. Laluet, and T. W. Ebbesen, “Channel Plasmon subwavelength waveguide components including interferometer and ring resonators,” Nature, vol. 440, no. 7083, pp. 508-511 (2006).

[29] R. Zia, M. D. Selker, P. B. Catrysse, and M. L. Brongersma, “Geometries and materials for subwavelength surface plasmon modes,” J. Opt. Soc. Am. A, vol. 21, no. 12, pp. 2442-2446 (2004).

[30] R. Zia, M. D. Selker, and M. L. Brongersma, “Leaky and bound modes of surface plasmon waveguides,” Phys. Rev. B, vol. 71, pp. 165431-1-9 (2005).

[31] G. Veronis and S. Fan, “Bends and splitters in metal-dielectric-metal subwavelength plasmonic waveguides," Appl. Phys. Lett., vol.87, 131102 (2005).

[32] G. Veronis and S. Fan, “Crosstalk between three-dimensional plasmonic slot waveguides," Opt. Express, vol. 16, no. 3, pp. 2129-2140 (2008).

[33] P. Berini, “Long-range surface plasmon polaritons,” Adv. Opt. Photon., vol. 1, no. 3, pp. 484-588 (2009).

[34] Fitrakis et al., “Slow light in insulator–metal–insulator plasmonic waveguides,” J. Opt. Soc. Am. B, vol. 28, no. 9, pp. 2159-2164 (2011).

[35] R. F. Oulton, V. J. Sorger, D. A. Genov, D. F. P. Pile, and X. Zhang, “A hybrid plasmonic waveguide for subwavelength confinement and long-range propagation,” Nat. Photonics, vol. 2, pp. 496–500 (2008).

[36] J. T. Kim, “CMOS-compatible hybrid plasmonic waveguide for sub wavelength light confinement and on-chip integration,” IEEE Photon.Technol. Lett., vol. 23, no. 4, pp. 206–208 (2011).

[37] D. Dai, and S. He, “A silicon-based hybrid plasmonic waveguide with a metal cap for a nano-scale light confinement,” Opt. Express, vol. 17, no.19, pp.16646–16653 (2009).

[38] D. Dai, and S. He, “Low-loss hybrid plasmonic waveguide with double low-index nano-slots,” Opt. Express, vol. 18, no. 17, pp. 17958–17966 (2010).

[39] M. Z. Alam, J. Meier, J. S. Aitchison, and M. Mojahedi, “Propagation characteristics of hybrid modes supported by metal-low-high index waveguides and bends,” Opt. Express, vol. 18, no.12, pp. 12971–12979 (2010).

[40] J. Wang, X. Guan, Y. He, Y. Shi, Z. Wang, S. He, P. Holmstrom, L. Wosinski, L. Thylen, and D. Dai, “Sub-μm^2 power splitters by using silicon hybrid plasmonic waveguides,” Opt. Express, vol. 19, no. 2, pp. 838–847 (2011).

[41] V. J. Sorger, Z. Ye, R. F. Oulton, Y. Wang, G. Bartal, X. Yin, and X. Zhang, “Experimental demonstration of low-loss optical waveguiding at deep sub-wavelength scales,” Nature Comm, vol. 2, no. 331, (2011).

[42] R. F. Oulton, V. J. Sorger, T. Zentgraf, R.M. Ma, C. Gladden, L. Dai, G. Bartal, and X. Zhang, “Plasmon lasers at deep subwavelength scale,” Nature, vol. 461, pp. 629–632 (2009).

[43] H. M. Gibbs, *Optical Bistability Controlling Light with Light* (Academic Press, Orlando, 1985).

[44] G. I. Papadimitriou, C. Papazoglou, and A. S. Pomportsis, "Optical Switching: Switch Fabrics, Techniques, and Architectures," J. Lightwave. Technol., vol.21, no. 2, pp. 384-405 (2003).

[45] G. M. Rebeiz, "RF MEMS switches: status of the technology," *the 12th International Conference on Solid State Sensors, Actuators and Microsystems*, 2003 Boston, pp. 1726-1729.

[46] S. Sharkawy, D. W. Prather, and R. A. Soref, "Electro-optical switching using coupled photonic crystal waveguides," Opt. Express, vol. 10, no. 20, pp. 1048–1059 (2002).

[47] M. Tian, P. Lu, L. Chen, D. Liu, and C. Lv, "All-optical switching in MIM waveguide resonator with an outer portion smooth bend structure containing nonlinear optical materials," Optics Communications, vol. 285, pp. 4562-4566 (2012).

[48] P. Muellner, M. Wellenzohn, and R. Hainberger, "Nonlinearity of optimized silicon photonic slot waveguides", Opt. Express, vol. 17, no. 11, pp. 9282-9287 (2009).

[49] B. A. Daniel, and G. P. Agrawal, "Vectorial nonlinear propagation in silicon nanowire waveguides polarization effects," J. Opt. Soc. Am. B/ Vol. 27, No. 5, pp. 956-965 (2010).

[50] N. A. Wolchover et.al, "High nonlinearity glass photonic crystal nanowires," Opt. Express, vol. 15, no. 3, pp. 829-833 (2007).

[51] H. Yin, C. Xu, and P. M. Hui, "Exact surface plasmon dispersion relations in a linear-metal-nonlinear dielectric structure of arbitrary nonlinearity," Appl. Phys. Lett., vol. 94, no. 22, art. 221102 (2009).

[52] R. Davoyan, I. V. Shadrivov, and Y. S. Kivshar, "Nonlinear plasmonic slot waveguides," Opt. Express, vol.16, no.26, pp. 21209-21212 (2008).

[53] D. Rukhlenko, A. Pannipitiya, and M. Premaratne, “Dispersion relation for surface plasmon polaritons in metal/nonlinear-dielectric/metal slot waveguides,” Opt. Lett., vol. 36, no. 17, pp. 3874-3876 (2011).

[54] X. Liu et.al, “Optical bistability in metal-insulator-metal plasmonic waveguide with nanodisk resonator containing Kerr nonlinear medium,” Appl. Opt., vol. 50, no. 27, pp. 5287-5290 (2011).

[55] Y. Shen, and G. P. Wang, “Optical bistability in metal gap waveguide nanocavities,” Opt. Express, vol. 16, no. 12, pp. 8421-8426 (2008).

[56] M. Wu, Z. Han, and V. Van, “Conductor-gap-silicon plasmonic waveguides and passive components at subwavelength scale,” Opt. Express, vol.18, no.11, pp. 11728-11736 (2010).

[57] S. Zhu, T. Y. Liow, G. Q. Lo, and D. L. Kwong, “Silicon-based horizontal nanoplasmonic slot waveguides for on-chip integration,” Opt. Express, vol.19, no.9, pp. 8888-8902 (2011).

[58] M. M. Hossain, M. D. Turner, and M. Gu, “Ultrahigh nonlinear nanoshell plasmonic waveguide with total energy confinement,” Opt.Express, vol. 19, no. 24, pp. 23800-23808 (2011).

[59] C. Milián, D. V. Skryabin, “Nonlinear switching in arrays of semiconductor on metal photonic wires,” App. Phys. Lett., vol. 98, art.111104 (2011).

[60] A. Pitilakis, O. Tsilipakos and E. E. Kriezis, “Nonlinear Effects in Hybrid Plasmonic Waveguides,” *14th International Conference on Transparent Optical Networks (ICTON)*, 2012 England, pp. 1-4.

[61] Y. Su, “Highly nonlinear ultrafast plasmonic waveguide device on SOI,” *Communication and Photonic Conference and Exhibition (ACP)*, 2010 Asia, pp. 732-734.

[62] M. N. Sadiku, *Numerical Techniques in Electromagnetics* (CRC Press Inc., Florida, 1992), pp. 407-440.

[63] COMSOL Multiphysics 4.2, 2011, COMSOL Inc. www.comsol.com.

[64] S. Lal, S. Link, N. J. Halas, “Nano-optics from sensing to waveguiding,” Nature Photonics, vol. 1, pp. 641-647 (2007).

[65] S. Afshar and T. M. Monro, “A full vectorial model for pulse propagation in emerging waveguides with subwavelength structures part I: Kerr nonlinearity,” Opt. Express, vol. 17, no. 4, pp. 2298-2318 (2009).

[66] P. B. Johnson and R. W. Christy, “Optical constants of the noble metals,” Phys. Rev. B, vol. 6, no. 12, pp. 4370-4379 (1972).

[67] Matlab version r2011b, The MathWorks Inc., 2011.

[68] J. M. Pitarke, V. M. Silkin, E. V. Chulkov, and P. M. Echenique, “Theory of surface plasmons and surface-plasmon polaritons,” Rep. Prog. Phys, vol. 70, no. 1, pp. 1-87 (2007).

[69] A. Yariv and P. Yeh, *Photonics Optical Electronics in Modern Communications,* 6th edition, (Oxford University Press, Inc, New York, 2007), pp. 137-138.

[70] A. Yariv, “Critical coupling and it control in optical waveguide-ring resonator systems,” IEEE Photon. Technol. Lett., vol. 14, no. 4, pp. 483-485 (2002).

[71] K. R. Hiremath, “Coupled Mode Theory Based Modeling and Analysis of Circular Optical Microresonators,” Doctoral Thesis, Twente University, Oct. 2005.